



**HAL**  
open science

# Interplay Between Fluid Intrusion and Aseismic Stress Perturbations in the Onset of Earthquake Swarms Following the 2020 Alex Extreme Rainstorm

Laetitia Jacquemond, Maxime Godano, Frédéric Cappa, Christophe Larroque

► **To cite this version:**

Laetitia Jacquemond, Maxime Godano, Frédéric Cappa, Christophe Larroque. Interplay Between Fluid Intrusion and Aseismic Stress Perturbations in the Onset of Earthquake Swarms Following the 2020 Alex Extreme Rainstorm. *Earth and Space Science*, 2024, 11 (6), pp.e2024EA003528. 10.1029/2024EA003528 . hal-04599818

**HAL Id: hal-04599818**

**<https://hal.science/hal-04599818v1>**

Submitted on 26 Sep 2024

**HAL** is a multi-disciplinary open access archive for the deposit and dissemination of scientific research documents, whether they are published or not. The documents may come from teaching and research institutions in France or abroad, or from public or private research centers.

L'archive ouverte pluridisciplinaire **HAL**, est destinée au dépôt et à la diffusion de documents scientifiques de niveau recherche, publiés ou non, émanant des établissements d'enseignement et de recherche français ou étrangers, des laboratoires publics ou privés.



Distributed under a Creative Commons Attribution - NonCommercial - NoDerivatives 4.0 International License

# Earth and Space Science



## RESEARCH ARTICLE

10.1029/2024EA003528

### Key Points:

- Multiple activation of small earthquake swarms after an extreme rainstorm in southern French Alps
- Bi-directional swarm migration velocities reveal an interplay between fluid diffusion and aseismic stress perturbations
- A stress-driven model explains the overall evolution of seismicity and provides insights into the triggering mechanisms

### Supporting Information:

Supporting Information may be found in the online version of this article.

### Correspondence to:

L. Jacquemond,  
laeticia.jacquemond@geoazur.unice.fr

### Citation:

Jacquemond, L., Godano, M., Cappa, F., & Larroque, C. (2024). Interplay between fluid intrusion and aseismic stress perturbations in the onset of earthquake swarms following the 2020 Alex extreme rainstorm. *Earth and Space Science*, 11, e2024EA003528. <https://doi.org/10.1029/2024EA003528>

Received 17 JAN 2024  
Accepted 17 MAY 2024





### Author Contributions:

**Conceptualization:** Laeticia Jacquemond, Maxime Godano, Frédéric Cappa  
**Formal analysis:** Laeticia Jacquemond  
**Investigation:** Laeticia Jacquemond  
**Methodology:** Maxime Godano, Frédéric Cappa  
**Supervision:** Maxime Godano, Frédéric Cappa, Christophe Larroque  
**Validation:** Laeticia Jacquemond, Maxime Godano, Frédéric Cappa, Christophe Larroque  
**Writing – original draft:** Laeticia Jacquemond

© 2024. The Author(s).

This is an open access article under the terms of the [Creative Commons Attribution-NonCommercial-NoDerivs License](#), which permits use and distribution in any medium, provided the original work is properly cited, the use is non-commercial and no modifications or adaptations are made.

## Interplay Between Fluid Intrusion and Aseismic Stress Perturbations in the Onset of Earthquake Swarms Following the 2020 Alex Extreme Rainstorm

Laeticia Jacquemond<sup>1</sup> , Maxime Godano<sup>1</sup> , Frédéric Cappa<sup>1</sup> , and Christophe Larroque<sup>1,2</sup> 

<sup>1</sup>Université Côte d'Azur, CNRS, Observatoire de la Côte d'Azur, IRD, Geoazur, Sophia Antipolis, France, <sup>2</sup>Université de Reims Champagne-Ardenne, GEGENA UR3795, Reims, France

**Abstract** The 2020 Alex storm in southern France led to localized extreme rainfall exceeding 600 mm in less than 24 hr. In the 100 days following the storm, a series of small earthquakes swarm occurred beneath the Tinée valley, a region characterized by a low background deformation. To gain insight into the mechanisms controlling swarm evolution, we used an enhanced seismic catalog to detect 188 events. These events exhibited magnitudes comprised between  $-1.03$  and  $2.01$ , and 78 of them were relocated using relative locations at an average depth of 3–4 km. Additionally, we estimated the directions and velocities of seismicity migration. Our analyses reveal multiple episodes of hypocenter expansion and migration within a fluid-saturated fault system. Observations provide evidence of a bi-directional seismicity migration marked by dual velocities within a swarm. The northward seismicity migration aligns with velocities indicative of aseismic slip ( $\sim 130$  m/hr), while the southward migration corresponds to velocities associated with fluid pressure diffusion ( $\sim 5$  m/hr). This migration pattern underscores the interplay of multiple physical mechanisms in both triggering and driving earthquakes. A stress-driven model based on rate-and-state friction successfully explains the overall evolution of observed seismicity, whereas a fluid-driven model fails to reproduce the data. Our observations and models suggest that fluid pressure changes resulting from intense rainfall caused aseismic slip in the shallow portion of the crust. We hypothesize that aseismic deformation serves as the driving force for the earthquake swarms, coupled with the invasion of pressurized fluid due to diffusing rainfall.

**Plain Language Summary** On 2 October 2020, the Alex storm caused extreme rainfall, exceeding 600 mm in less than 24 hr, in southern France. Subsequently, 188 earthquakes were recorded, and 78 of them were precisely relocated at depths of 3–4 km beneath the Tinée valley in the 100 days following the storm. Such increased seismic activity is unusual in this region characterized by low deformation ( $<1$  mm). Using seismic data, we identified two directions of seismicity migration marked by dual velocities within swarms—one indicative of aseismic slip, and the other corresponding to fluid pressure diffusion. A purely fluid-driven model fails to accurately reproduce the temporal evolution of seismicity, while observed data are effectively modeled based on intermittent stress changes resulting from a slow aseismic slip. Our investigations lead us to attribute earthquake activity to aseismic deformation, acting as the driving force for the swarms, coupled with the invasion of pressurized fluid due to infiltrating precipitation.

## 1. Introduction

Most of the time, earthquakes typically originate from geological processes. These earthquakes are caused by tectonic stresses that load a fault until the accumulated elastic energy is suddenly released in a seismic rupture (Reid, 1911; Scholz, 2019). Additionally, fluids diffusing in the crust can also induce stress variations, impacting the faults directly (Cappa et al., 2019; Hainzl, 2004; Miller, 2013; Scholz, 2019). Previous studies have unveiled crustal deformations linked to hydraulic forcing in diverse tectonic settings. For instance, in the Matsushiro volcanic area in Japan, Cappa et al. (2009) successfully demonstrated the correlation between upwelling fluid sources and swarm activity. Independently, Bollinger et al. (2007) and Johnson et al. (2017a, 2017b) showcased the role of seasonal variations in rainfall in modulating seismicity rates along plate boundary regions in Nepal and California. Globally, the influence of increased fluid pressure or surface hydrological loading on the triggering of the intraplate seismicity has been explored, as evidenced by studies such as those by Costain (2017) and Craig et al. (2017). These observations underscore that deformations induced by variations in surface loads, the

Writing – review & editing:  
Maxime Godano, Frédéric Cappa,  
Christophe Larroque

infiltration of water into the ground or ascendent fluid intrusions, have the capacity to disrupt the stress conditions and fluid pressure within subsurface fault systems, leading to seismicity.

Compelling evidence exists for seismic activity associated with climatic forcing (Wilson et al., 2022), which can cause stress variations on crustal faults that in some conditions can facilitate the occurrence of earthquakes, depending on the level to which the external stress perturbations align with the background tectonic stress regime. It has been reported that surface processes, such as ice and snow load, heavy rainfall, atmospheric pressure, and surface temperature, seasonally modulate seismic activity in the crust (Bettinelli et al., 2008; Costain & Bollinger, 2010; Hsu et al., 2021; Johnson et al., 2017a, 2017b; Montgomery-Brown et al., 2019). For instance, relationships between intense rainfall and earthquakes have been previously studied to evaluate the triggering and seasonal modulation of seismicity by meteorological conditions at local and regional scales (Bollinger et al., 2007; Chmiel et al., 2022; Christiansen et al., 2007; Costain et al., 1987; Hainzl et al., 2006, 2013; Husen et al., 2007; Miller, 2008; Rigo et al., 2008). Studies have found that in regions dominated by extensively fractured and permeable rocks, typically karst geological settings, if enough rain permeated the ground and increased thickness of the water table, it could change the stress on critically stressed faults and hence trigger earthquakes (D'Agostino et al., 2018; Hainzl et al., 2006; Husen et al., 2007; Kraft, Wassermann, & Igel, 2006; Rigo et al., 2008; Roth et al., 1992; Perrochet et al., 2023). In these scenarios, the time lag between the peak rainfall and the onset of increased seismic activity can be hours, days or weeks. For instance, Husen et al. (2007) documented a series of earthquakes in Central Switzerland triggered in August 2005 at the end of a 3-day period of exceptional heavy rainfall. Montgomery-Brown et al. (2019) also documented a series of seismic swarm events in the upper few kilometers of the crust near Long Valley Caldera in California, which coincided with peak stream flows following snowmelt, showing an average delay of 3–4 weeks.

However, the connection between seismic activity and water forcing due to rainfall is subtle and does not systematically appear. The scarcity of data frequently results in ambiguous interpretations (Wilson et al., 2022). In most cases, the seismicity evolution associated with rainfall occurs as a swarm (i.e., small magnitude earthquakes without mainshock) (Costain & Bollinger, 2010; Kraft, Wassermann, Schmedes, & Igel, 2006). There is no evidence that large, destructive earthquakes are induced by rainfall. However, periods of heavy rainfall might affect the stability of active fault systems. Important questions remain on the physical mechanisms involved, such as understanding whether and how rainwater can directly change stress on faults located at several kilometers below the earth's surface to the depths where most earthquakes occur, and how the faults respond.

Here, we focus on earthquake swarms in the Tinée valley, Southern French Alps, following the extreme rainfall caused by the devastating Alex storm, which occurred on 2 October 2020 (Carrega & Michelot, 2021; Chmiel et al., 2022). This very intense storm lasted for less than 24 hr, and generated up to 600 mm of rain locally. In the Tinée valley, the spatial coincidence between the seismic sequences and the maximum rainfall of the Alex storm (Chmiel et al., 2022) provides a unique insight into the physical mechanisms involved. In this paper, we study the interplay between fluid infiltration, stress perturbation, and seismic activity. First, we used seismological data to examine the spatio-temporal evolution of multiple earthquake swarms over a 100-day period following the storm, while also examining focal mechanisms in conjunction with the geological context. Then, to investigate possible processes triggering and driving the swarm sequences, we model the temporal evolution of seismicity using stress changes due to rainfall and from a slow aseismic slip event using a stress-driven model based on rate-and-state friction. Finally, we discuss the causal relationship between extreme rainfall, fluid pressure diffusion from water infiltration, intermittent stress perturbation from slow slip and swarm seismicity associated with this extreme meteorological event.

## 2. The 2020 Extreme Rainstorm in the Southern French Alps

On 2 October 2020, an extreme meteorological event, known as the “Alex storm” struck the French southwestern Alps, with a particular impact on the lower Tinée valley. Originating in the northern part of the Atlantic Ocean, this storm exploited a convergence of favorable meteorological conditions in the Mediterranean Sea, intensifying its rainfall front over the region (Carrega & Michelot, 2021).

In less than 24 hr, certain areas experienced more than 600 mm of rainfall, marking the highest daily precipitation since 1997 (i.e., the beginning of the regional rainfall measurements) and exceeding the annual average (Chmiel et al., 2022). This unprecedented torrential rainfall resulted in widespread flash floods and landslides, leading to numerous casualties and damages, particularly in the Tinée valley (Figure 1). The intensity of this storm was not

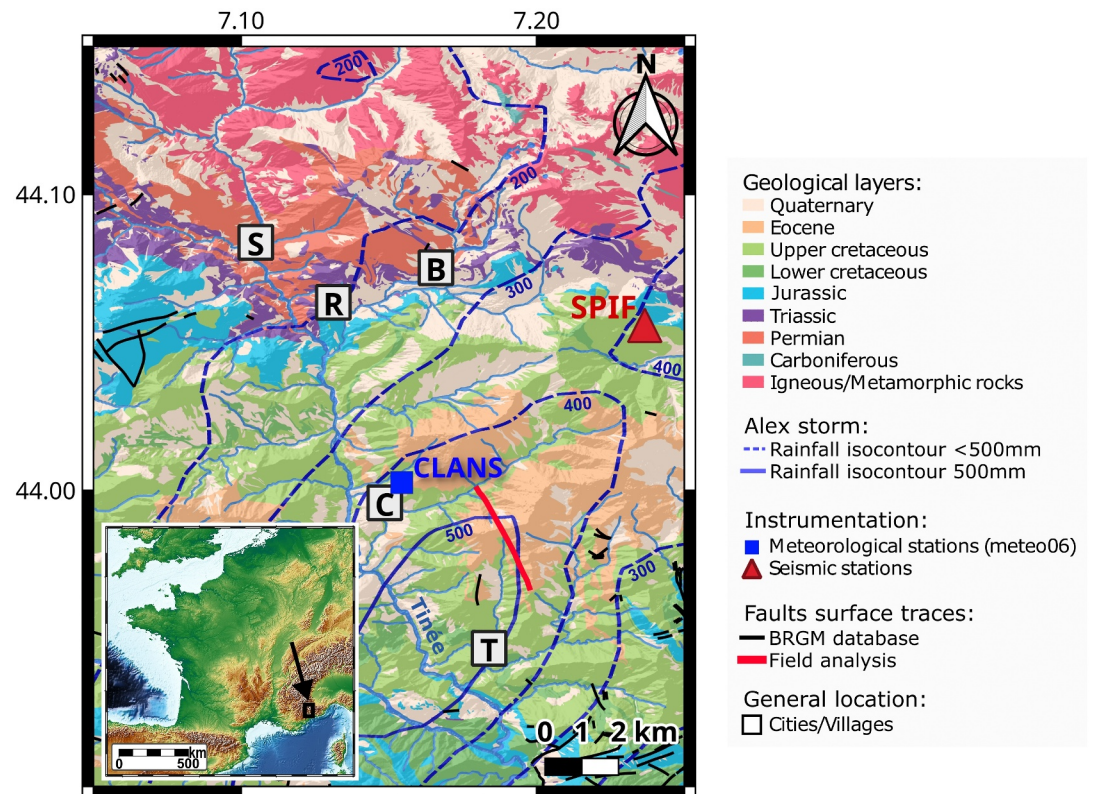


**Figure 1.** A simplified geological map of the studied area (source from <http://infoterre.brgm.fr/>, 2023), with the surface traces of main faults in the lower Tinée valley, located in the southern French Alps. The map incorporates blue isolines denoting the quantity of rainfall recorded during the 2020 Alex storm. The thickest line corresponds to 500 mm, with dashed lines indicating 100 mm-decreasing quantity of rainfall (e.g., 400, 300 mm, etc.). The positions of meteorological and seismological stations are also indicated. Pink squares refer to villages with abbreviations indicating specific locations: S = Saint-Sauveur-sur-Tinée, R = Rimplas, B = La Bolline, C = Clans, T = La Tour.

expected, given its rarity in the region, as evidenced by a long return period. Carrega and Michelot (2021) calculated some recurrence intervals ranging from hundreds to thousands of years, underscoring the exceptional nature of this event.

The extreme nature of this meteorological event stems from the convergence of a substantial amount of rainfall (>600 mm) over a short period (<24 hr). In comparison, two previous rainfall events occurred in the same region in 2015 and 2019, with only localized rainfall exceeding 100 mm in less than 3 hr (Brigode et al., 2021). Noteworthy, in South of France, is the occurrence of extreme floods during a “Cevenol episode” in September 2002 in Nimes, in similar meteorological conditions (~600 mm in 28 hr) (Delrieu et al., 2005). The severity of the Alex storm becomes even more apparent when compared to other recent global flood events over the world. Notable examples include unusual rainfall of 240 mm in the Tokyo region on 12 October 2019, associated with the typhoon Hagibis (Li & Otto, 2022), hourly rainfall accumulation reaching up to 400 mm associated with the cyclone Gabrielle in the northern island of New-Zealand, resulting in destructive floods (Harrington et al., 2023), and 900 mm recorded in 72 hr in Vietnam in December 2018 (Wang & Nguyen, 2023).

Despite a limited number of intense rainfall in France, Ribes et al. (2019) draw attention to an “intensification of the most extreme events over the last decades” in the French Mediterranean area, encompassing factors such as frequency, intensity, extent and precipitated volumes. More recently, in September 2023, torrential rainfall followed by destructive floods successively affected Spain, Greece, Bulgaria and Libya in the Mediterranean region, capturing the interest of the scientific community.

### 3. Seismotectonic Setting of the Southwestern French Alps

The southwestern French Alps present a diverse tectonic inheritance (Larroque et al., 2021) shaped by a succession of distinct tectonic phases. Following a Mesozoic period characterized by rifting and spreading phase, the convergence of the European plate and the African plate developed during the late Cretaceous. This convergence led to the successive subduction of the Tethys Ocean, followed by the northern margin, and finally the collision of the Adriatic microplate and European paleomargins (Dercourt et al., 1986; Handy et al., 2010; Stampfli et al., 1998). The crustal shortening started around 50 Ma (Eocene) and ended up 3 Ma (Pliocene) as the deformation of the chain propagates from the inner part of the chain toward the external part. This shortening was maintained by successive orogenic phases (Coward & Dietrich, 1989; Dumont et al., 2022), marked by Miocene and Plio-Pleistocene extension within the inner part of the chain (Sue & Tricart, 2003). In the southernmost part of the chain, the Ligurian oceanic basin opened during late Oligocene-early Miocene times as a back-arc basin generated from the southeastward roll-back of the Apennines-Maghrebides subduction zone (Gattacceca et al., 2007; Jolivet et al., 2008). This results in a fan-shaped geometry of the chain, adapting the anticlockwise rotation of the Adria microplate. The more recent south-westernmost section of this microplate is concurrently accommodating both the Neogene Apenninic slab roll-back and the Ligurian basin opening (Eva et al., 2020).

In spite of the end of its orogenic phase, the southwestern part of the Alps remains a seismically active region, exhibiting low deformation rates of less than 1 mm of convergence per year (Calais et al., 2002; Eva et al., 2020; Larroque et al., 2009; Nocquet, 2012). Recent GNSS strain rate measurements and stress inversion analyses have revealed a broad spectrum of stress values and orientations within the area (Masson et al., 2019; Walpersdorf et al., 2018).

Despite the relatively low rates of tectonic deformation in the region, the seismicity is considered as moderate, as indicated by historical events and instrumental records (Larroque et al., 2021). Notably, several earthquakes with magnitude ranging from 4 to 6 have occurred at depth of less than 20 km, particularly in proximity to densely populated areas in the southwestern Alps and the Ligurian coast. A diversity of seismic behaviors is observed, each attributable to distinct driving processes (Larroque et al., 2021). Fluids play a crucial role in these processes, contributing, for instance, to the migration of high fluid pressure front in the Sampeyre swarm (Godano et al., 2013). In some cases, fluids combine with other physical processes such as coseismic stress transfer, fluid pressure diffusion and distant stressing, to trigger an aftershock sequence, as observed in the Ubaye region in 2014 (De Barros et al., 2019). Notably, fluids may also explain a portion of the seismicity in the Argentera Massif, north of the Tinée valley, where Baietto et al. (2009) presented a complex conduit system involving fault-valving mechanisms.

In this study, we focus on the Tinée valley, located 35 km north of the city of Nice. Rising in the Argentera-Mercantour massif, the Tinée river flows for 70 km. In its lower part, the valley, oriented N170°, cuts through the Eocene/Cretaceous/Jurassic sedimentary layers (Figure 1), known for a historically low seismic rate. Between 2014 and 2020, only 138 events, with local magnitudes ranging from 0.28 to 3.39 were recorded in this region (<https://sismoazur.oca.eu>). However, in the hours following the flash flood caused by the Alex Storm, there was a significant increase in the seismic activity. Over the subsequent 2 months, the permanent seismological network detected 23 earthquakes, with magnitudes ranging from 0.6 up to 2.01—a notably unusual seismicity rate for the region since 2014. Additionally, Chmiel et al. (2022) identified 91 additional events using template matching. They used the initial 23 events as templates, and scanned the continuous signal of the MVIF station (Figure S1 in Supporting Information S1) on the October–December 2020 period.

## 4. Seismicity Data and Methods

### 4.1. Seismological and Meteorological Data

The seismic activity in the southwestern French Alps is recorded by the French (RESIF, 1995) and Italian (University of Genoa, 1967; Istituto Nazionale di Geofisica e Vulcanologia (INGV), 2005) (permanent seismological networks). Since 2014, the seismicity is permanently monitored by the seismological observatory of Observatoire de la Côte d'Azur hosted by the Géoazur laboratory, utilizing the SeisComp3 system (seiscomp3-jakarta-2018.327, Hanka et al., 2010). Earthquakes are automatically detected using the short-time average—long-time average (STA/LTA) routine integrated in the module SCAUTOPICK of SeisComp3 (signal filtered between 4 and 10 Hz and STA/LTA ratio of 1/30). The P- and S-waves of the events are then manually re-picked

with a webpicker developed internally in Geoazur laboratory (available at <https://gitlab.oca.eu/cheze/webpicker>), and the events are subsequently located in IASP91, using LOCSAT through the webpicker. Earthquakes are then listed in the Sismoazur data set that contains more than 7,600 earthquakes, with local magnitudes  $M_{IV}$  ranging from  $-0.73$  to  $5.03$  (estimated by SCMAG from SeisComp3).

This study utilizes 14 seismological stations from both the French (CALF, ENAUX, ESCA, ISO, JAUF, MVIF, SALSA, SAOF, SPIF, SURF, TRIGF, TURF) and Italian (ENR, STV) networks (Figure S1 in Supporting Information S1). These stations were selected based on their favorable azimuthal gap concerning seismicity ( $47^\circ$ – $163^\circ$ ) and their proximity to the seismic events ( $2$ – $75$  km). The stations predominantly consist of high-gain seismometers, with sampling rate of  $100$  Hz. All the stations were installed prior 2014, and have continuously recorded seismic activity since that time.

Furthermore, rainfall data in the lower Tinée valley are recorded through rain gauges. Due to availability consideration, open-source data from the rain gauge operated by the Nice Meteo 06 association, particularly the Clans station, have been used. This station, operational since 16 January 2016, stands at an elevation of  $665$  m on top of an  $8$ -m pole. It is the closest ( $\leq 3$  km) to the areas experiencing the heaviest rainfall ( $>600$  mm), and is located less than  $1.5$  km from the epicenters of the main seismic activity observed in the days following the Alex storm.

The Clans station is a Davis Instruments Vantage Pro 2 Plus weather station, equipped with a tipping bucket for rainfall measurements, along with other meteorological sensors for humidity, wind, and temperature. It provides measurements every  $\sim 20$  s, with a precision of  $\pm 5\%$  for rainfall intensities up to  $250$  mm/hr. The rain-catching surface, measuring  $214$  cm<sup>2</sup>, allows the reservoir to capture up to  $762$  mm per hour before tilting to discharge the water and returning to its initial position. Data collected every minute by a Raspberry Pi and the Weewx software are automatically transmitted to the Nice Meteo 06 database.

## 4.2. Seismicity Detection

A comprehensive examination of seismic clusters in the lower Tinée valley, including their location, geometry, and temporal activity, is developed to (a) precisely understand how the seismicity activated following the Alex storm aligns with the seismotectonic context (i.e., faults, geological layers), and (b) understand if some of these clusters may have links with the intense rainfall. To achieve this, the creation of an exhaustive catalog of seismicity covering an extended period with highly precise location data is essential. To this aim, as a first step, template matching was employed for the period between 2014 and mid-2022. This initial phase aimed to detect additional low-magnitude earthquakes that might have been overlooked by the STA/LTA method, thereby expanding the Sismoazur data set.

The template matching (e.g., Gibbons & Ringdal, 2006) is a widely used method to detect low magnitude earthquakes in continuous seismological recordings. In this study, we use the following approach. Template matching is only performed on the vertical component of the recordings to decrease the processing time. Data are bandpass-filtered in the  $5$ – $40$  Hz frequency range to remove low and high frequency noises. Template windows include both P- and S- waves, with the beginning time taken  $0.3$  s before the P-wave onset and the ending time  $3$  s after the S-wave onset. Each template is cross-correlated with the daily recordings of the three nearest (mean distance between the stations and the seismicity:  $\sim 15$  km) seismological stations (MVIF, SPIF, ISO) over the period from 1 January 2014 to 15 August 2022. An overlapping sliding window of  $25\%$  of the template window is used to scan the continuous data. When the cross-correlation coefficient between the template and the window of continuous signal is greater than, or equal to,  $0.6$ , a new detection is defined. We have chosen this threshold value of  $0.6$  to detect events slightly different from the templates (Chmiel et al., 2022), while avoiding too many false detections. The local magnitude of a new detection is estimated from the ratio between its maximum amplitude and the maximum amplitude of the template with which it best correlates, as follows:

$$M_L^{\text{detec}} = \log_{10} \left( 10^{M_L^{\text{temp}}} \times \frac{A_{\text{max}}^{\text{detec}}}{A_{\text{max}}^{\text{temp}}} \right) \quad (1)$$

Within the study zone (longitude  $7.00$ – $7.25$ ; latitude  $43.90$ – $44.13$ ),  $138$  earthquakes have been listed in the Sismoazur data set since 2014 (referred to hereafter as the “*original data set*”). Some of these earthquakes exhibit similar waveforms, suggesting nearby location with slightly different focal mechanisms and closely aligned

raypaths. Utilizing them as templates could result in redundant detections. To speed up the execution of the template matching procedure, we classify the 138 events in clusters using waveform similarity criteria. The classification methodology is detailed in Supporting Information S1 (Text S1, Figures S2 and S3). Finally, a total of 86 templates are designed as the maximum magnitude event within each cluster (26 templates), plus 60 remaining isolated earthquakes (not classified into any cluster).

### 4.3. Seismicity Location

The original data set, along with the newly detected earthquakes, are precisely located using the double-difference method and the HypoDD software (Waldhauser & Ellsworth, 2000). This location process is performed using data from the 14 closest stations within the French and Italian networks. Prior to initiating this location, some preliminary steps are required.

First, P- and S- waves picking of the original data set have been carefully re-evaluated to enhance precision, resulting in mean manual picking uncertainties of  $P \sim 0.03$  s and  $S \sim 0.07$  s.

Subsequently, the original data set, initially localized by Sismoazur using the iasp91 Earth model (Kennett & Engdahl, 1991), is relocated with a more suitable regional velocity model (Eva et al., 2001). This 8-layer 1-D model is designed for depths up to 80 km. For further details, the entire model is available in Supporting Information S1 (Table S1). This relocation step is crucial to improve the accuracy of the location of the original data set, which then serves as the initial location for the subsequent double-difference relocation step (see below). The relocation is executed using the NonLinLoc software (Lomax et al., 2000, 2014).

HypoDD software enables the use of P- and S- delays computed by cross-correlation for pair of events (cross-correlation times). This prior requires defining cross-correlation windows encompassing P- and S-waves for each earthquake at each station. This is straightforward for the original data set since the P- and S- arrival times are already known. However, for the new detections, the determination of P- and S- arrival time is required to correctly set correlation windows. The quantity of events detected by template matching (515) makes tedious the manual picking of P- and S-waves. Therefore, this step is achieved by using the automatic picker General seismic Phase detection (Woollam et al., 2022) as described in Supporting Information S1 (Text S2; Figure S4). Next, the length of the cross-correlation window is set for the P-wave as 1.3 s (0.6 s before the arrival time and 0.7 s after) and for the S-wave as 2.5 s (0.5 s before the arrival time and 2 s after). Lastly, the double-difference relative location is carried on.

For the original data set, P- and S- delays of manual picking between pairs of events (catalog times) and P- and S-cross-correlation times are both used in the location determination. For new detections, only cross-correlation times are used. The initial location of new detections is set as the location of their best templates. To enhance accuracy, the double-difference location is also performed in the regional velocity model of Eva et al. (2001). The details of parameters set for the location are described in Supporting Information S1 (Text S3; Table S2). Following the approach of Waldhauser and Ellsworth (2000), the double-difference location uncertainties are assessed by a bootstrap resampling method of residual times arising from the final locations. Earthquakes are then relocated with these sampled data. This process is repeated 200 times and the 95%-distribution of the cumulative bootstrap relocations gives an estimation of the relative uncertainties in X-, Y-, and Z-directions.

### 4.4. Focal Mechanisms and Local Stress Inversion

In order to determine the geometry of the seismogenic structures, especially those activated after the extreme rainfall of the Alex storm, focal mechanisms are calculated by inverting both P-wave polarities and S/P amplitude ratios following the method of Godano et al. (2009, 2014). The main objective of the inversion is to retrieve the best double-couple focal mechanism following a simulated annealing exploration of three parameters: the fault plane azimuth, dip and rake angle. Uncertainties on the focal mechanisms are determined considering both the uncertainties in events locations, and the uncertainties associated with the amplitude measurements. One hundred new inversions are conducted, incorporating perturbations in amplitudes and event locations. These perturbations are sampled from a Gaussian distribution with a standard deviation equal to the amplitudes and locations uncertainties.

P-wave polarities and S/P amplitude ratios provided to the inversion are picked based on the following procedure. The P-wave polarity is picked on the vertical component of the signal. For the P- and S-, the first motion

amplitude is measured on the three components (N for north-south, E for east-west and Z for the vertical component). P- and S- amplitudes are defined as the Euclidian norm of the first motion amplitudes measured on the three components as  $A = \sqrt{(A_N^2 + A_E^2 + A_Z^2)}$ , with A the amplitude of P- or S-wave, and  $A_N, A_E, A_Z$  the amplitudes measured on the three components of the signal for P- or S-wave.

Focal mechanisms have been calculated for the located events with the strongest magnitudes, ranging from 1.39 to 3.39. These events have the best signal/noise ratio to reduce the uncertainties in the polarities and amplitudes picking process. Thirty-one focal mechanisms have been calculated from the new catalog over the 2014–2022 period, including eight mechanisms belonging to events occurring during the Alex storm. Using the Focal Mechanisms Classification (FMC) from Álvarez-Gómez (2019), those mechanisms are then classified into seven categories (normal, normal-strike-slip, strike-slip-normal, strike-slip, strike slip-reverse, reverse-strike slip, reverse) depending on the value of their P, T, B Centroid Moment Tensor axes.

Lastly, a local stress tensor is then calculated based on the inversion of the focal mechanisms following the MSATSI method from Hardebeck and Michael (2006) and Martínez-Garzón et al. (2014). Uncertainties in the stress inversion are determined using the method of Baques et al. (2023). While Martínez-Garzón et al. (2014) solely employ bootstrap resampling approach of the focal mechanisms to assess stress tensor uncertainties, Baques et al. (2023) create 100 new subsets of focal mechanisms by randomly perturbing the original solutions. Perturbations are drawn from a Gaussian distribution with standard deviation equal to the uncertainties of the focal mechanisms. These new subsets are then inverted, and the dispersion of the principal stresses enables to estimate their uncertainties.

## 5. Spatio-Temporal Evolution of Seismicity Following the Heavy Rainfall Associated With the 2020 Alex Storm

### 5.1. Seismicity Over the Period 2014–2022

As previously mentioned in the seismotectonic context (Section 3), the lower Tinée valley exhibits a low seismicity rate, with only 138 events detected through permanent networks from 2014 to 2022. Employing the template matching over an extensive 8-year period has detected additional earthquakes. Figure 2 shows the resulting data set composed of 515 new events (those detected by template matching) with magnitude ranging from  $-1.49$  to  $1.66$ , plus the 138 events of the original data set. Note the template matching has retrieved for the period October–December 2020, the events initially detected by Chmiel et al. (2022). The seismicity is characterized by the alternation of quiet (with on average 3 earthquakes/month) and more intensive seismic periods like in 2016 and 2020–2021, with peak of almost 160 earthquakes per month in autumn 2020, following Alex storm.

To ensure robust relative location accuracy, stringent criteria (Text S3 in Supporting Information S1) were applied, resulting in the precise localization of 266 events out of the 653 detected. Horizontal and vertical double-difference location uncertainties (i.e., uncertainties inside the cloud of seismicity) are estimated at  $X \sim 50$  m,  $Y \sim 80$  m and  $Z \sim 125$  m, respectively. Figure 3a presents these new event locations, with black dots indicating the seismicity in the days following the heavy rainfall of Alex storm (from October to December 2020), while the white dots represent all other events between 2014 and mid-2022. The seismicity predominantly impacts the left riverbank of the Tinée, consistently situated 1–2 km eastward from the main stream. The overall trend of the seismicity aligns  $N160^\circ$ – $N170^\circ$ , sub-parallel to the main orientation of the valley. Examining the seismicity distribution around the latitude  $44.05$ , close to swarms C and D (Figure 3), a second orientation ( $\sim N70^\circ$ ) quasi-perpendicular to the main orientation of the Tinée valley is visible. The seismicity from the right riverbank of the Tinée river, located at latitude  $44.03$  and longitude  $7.09$  (Figure 3a), tends to align with La Bolline Valley, located east of Rimplas.

Although the average depth of seismic activity post-Alex storm is situated around 4 km depth (Figures 3b and 3c), an examination of the seismicity distribution from 2014 to 2022 along a longitudinal South-North cross-section of the valley (Figure 3b) reveals a northward gradual increase in the focal depths from 4 to 10 km.

The primary types of focal mechanisms are mainly normal and reverse, with a minor strike-slip component (Figures S5 and S6 in Supporting Information S1). The nodal planes globally exhibit bimodal strike with a predominant N-S to NW-SE direction ( $N180^\circ$ – $N150^\circ$ ), and a secondary east-west direction ( $N70^\circ$ – $N90^\circ$ ). The



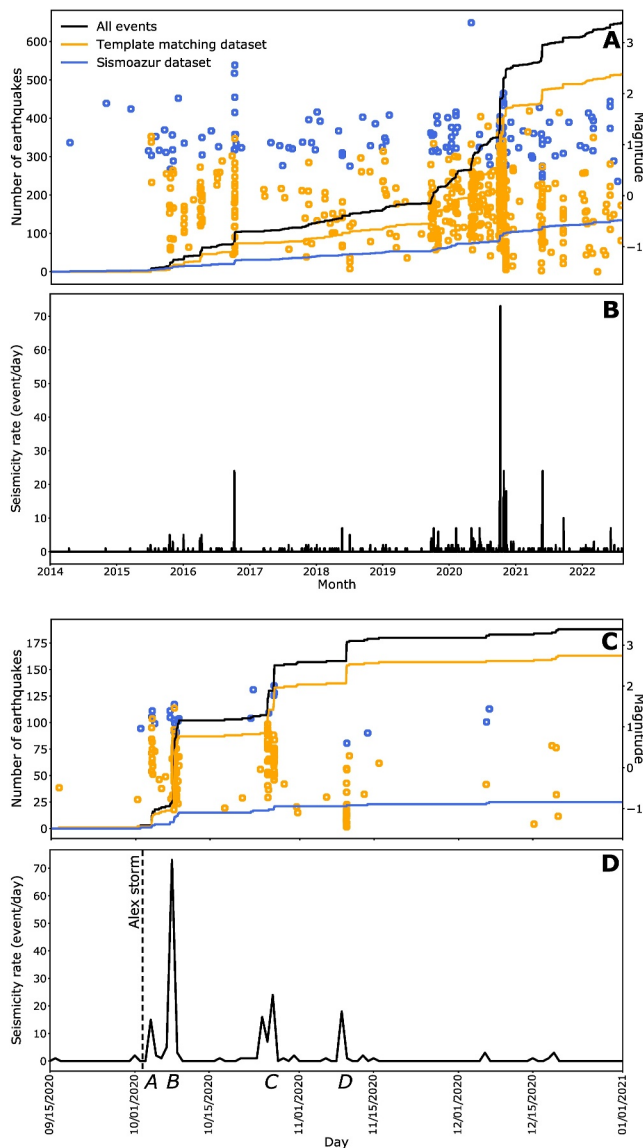


**Figure 2.** Histograms of the seismicity: (a) Cumulated number of events detected between 2014 and 08/2022, (b) Daily seismicity rate from 2014 to 08/2022, (c) Cumulated number of events detected from 09/15/2020 to 01/01/2021, (d) Daily seismicity rate from 09/15/2020 to 01/01/2021. Blue bars represent the original seismicity of the Sismoazur data set, while the orange bars denote the seismicity detected by the template matching. The magnitudes associated to those events are indicated by circles. Swarms identified in Figure 3 are labeled A, B, C, and D. Note: Only a limited number of these events have been precisely relocated using double-difference HypoDD method.

northwest-southeast normal-fault solutions systematically have a steep dipping nodal plane (ranging from 63°–88°). The other focal mechanisms are rather heterogeneous in dip and strike. Spatially, while a swarm active in October 2016 between Clans and Rimplas villages shows a prevalence of N-S to NW-SE normal-fault mechanisms, the other areas display a mix of focal mechanisms. La Bolline valley, which crosscuts the Tinée valley at 44.05°N, exhibits almost only reverse mechanisms, with nodal planes oriented N70–90°. These results suggest the development of a N160–170° subvertical faults network along the Tinée valley, crosscut by conjugate faults striking N70–90°, like in la Bolline Valley.

Ultimately, the orientations of the local stress axis ( $\sigma_1 \sim N165^\circ$ ,  $\sigma_2$  quasi-vertical, and  $\sigma_3 \sim N75^\circ$ ), derived from the inversion of the nodal planes (Figure S7 in Supporting Information S1), are in good agreement with prior studies (Baroux et al., 2001; Ritz, 1992). The strike-slip regime identified in this area is consistent with the conceptual seismotectonic model proposed by Eva et al. (2020), indicating right-lateral slip along NNW-SSE to WNW-ESE high-angle faults associated with shortening in the southern external zone.

## 5.2. Focus on the Earthquake Swarms Following the Rainfall

The template matching conducted over the period 2014–2022 shows no evidence of seismic swarm reactivation during the Alex storm period. There is no detection of new events in the October–December 2020 period when employing templates from periods preceding or following the Alex storm.

Consistent with the observations of Chmiel et al. (2022), the storm is followed by multiple seismic sequences, evident in the histogram of the number of detections through time (a total of 188 events detected (3 events detected between 15 September 2020, and 185 events detected in the 100 days following the storm) with magnitudes range from  $-1.03$  to  $2.01$ ; Figures 2c and 2d). A few events are detected 2 days after the storm, followed by a substantial seismic sequence 6 days later. A multi-peaks sequence of seismic activity is highlighted on 25th–27th October 2020, with a final sequence occurring on 9 November 2020. Some sparse events also occurred within this period; their quantity is not comparable to the swarm sequences.

Among the four main swarms depicted in Figure 2, which occurred shortly after the Alex storm, denoted as swarms A (4th October 2020), B (8th October 2020), C (25th–27th October 2020), D (9th November 2020), we will focus on swarm B (8th October 2020). This swarm, concentrated into a cluster near the Clans village (Figure 3a) is of particular interest. Notably, we lacked a sufficient number of located events for the remaining swarms (only 20 and 10 events for the two largest), on the 78 events relocated using double differences out of the 188 events detected, which precludes us for drawing conclusive insights regarding their geometry.

The seismic sequence within swarm B, comprising 42 located earthquakes, is trending  $\sim N170^\circ$  (Figure 4). The majority of seismicity is located at 3.6 km

depth. Examination of both the along-plane ( $N170^\circ$ ) and perpendicular-to-the-plane ( $N80^\circ$ ) cross-sections reveals an apparent plane of seismicity measuring approximately 400 m long and 200 m high, with a steep dip to the east. The optimal plane that best fits the distribution of seismicity is oriented at  $N150^\circ$  with a dip angle of  $75^\circ$  in the eastward direction. However, considering the vertical uncertainty of the relative location, which is approximately 125 m, comparable to the vertical extent of swarm B, we conclude that it represents a seismic lineament rather than a distinct seismic plane. The strike of swarm B is consistent with the subvertical local fault network evidenced in the meso-cenozoic sedimentary cover of the lower Tinée valley (i.e., fault surface trace in Figure 1 from field analysis). Additionally, its orientation is consistent with the direction of the major faults observed in the

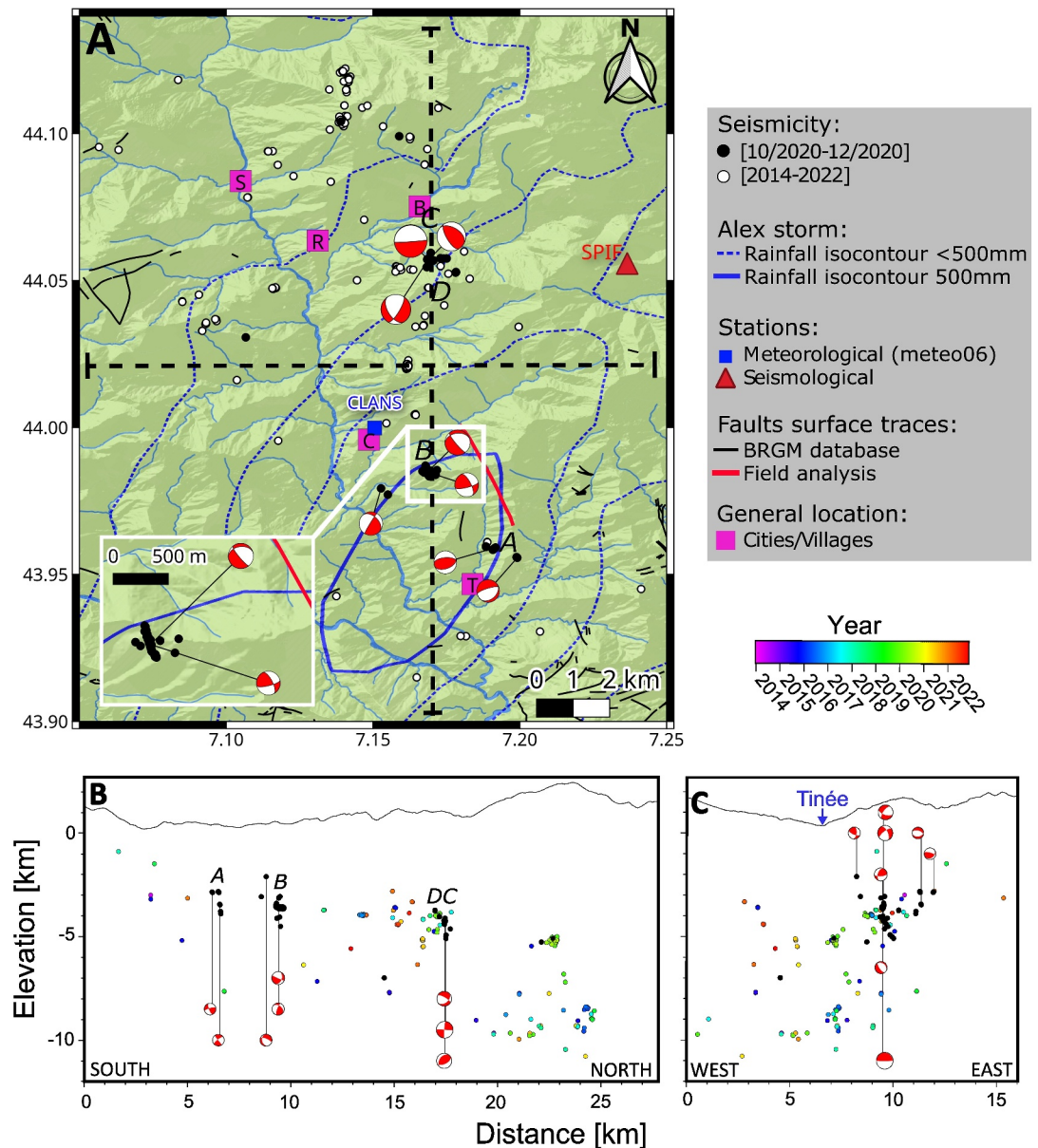


**Figure 3.** (a) Maps illustrating the distribution of seismicity in the lower Tinée valley, with its new precise double-difference location and associated focal mechanisms. The isolines depicting rainfall from the 2020 Alex storm are also included. South-north (b) and west-east (c) cross-sections of the seismicity of the whole valley are presented. White dots indicate the seismicity over the 2014–2022 period, except the October–December 2020 seismicity shown in black. The red triangle represents the position of seismological stations, while the blue square marks meteorological stations. Magenta squares represent the main villages.

crystalline basement of the Argentera Massif, situated north of the Tinée valley, including the active Bersezio fault (Larroque et al., 2001). The strike of swarm B is further in agreement with the main stress orientations ( $\sigma_1 = N166^\circ \pm 27^\circ$  dipping  $39^\circ \pm 24^\circ$ ,  $\sigma_2 = N345^\circ \pm 35^\circ$  dipping  $63^\circ \pm 25^\circ$ ,  $\sigma_3 = N255^\circ \pm 15^\circ$  dipping  $7^\circ \pm 15^\circ$ ) and the  $\sim N165^\circ$  subvertical nodal plane of the focal mechanism. Consequently, we interpret this seismic alignment as the intersection between a subvertical fault striking at  $N170^\circ$  and a second subparallel fault (or a major lithological limit).

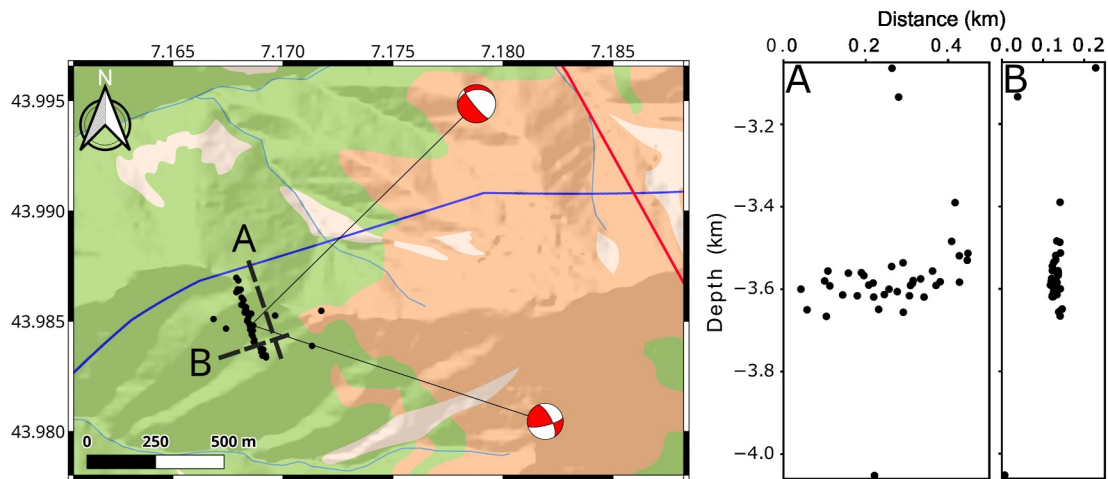


**Figure 4.** Close-up view on swarm B triggered 6 days after the 2020 Alex storm (2nd October 2020) with its associated focal mechanisms. The red line represents a surface trace of the fault identified in the field by geological observations. (a) North-south and (b) west-east cross-sections showing the seismicity migration within the swarm.

### 5.3. Seismicity Migration

The locations of earthquakes of the post-Alex storm seismic sequence (October–December 2020) as a function of time (top panel in Figure 5) clearly exhibits a northward successive activation of the swarms A, B, and C at an approximate velocity of 500 m per day. This corroborates the observations previously discussed by Chmiel et al. (2022). The first swarm is triggered in the area experiencing the highest rainfall levels (>500 mm, Figure 3), and then swarms spread to areas receiving less than 500 mm of rainfall.

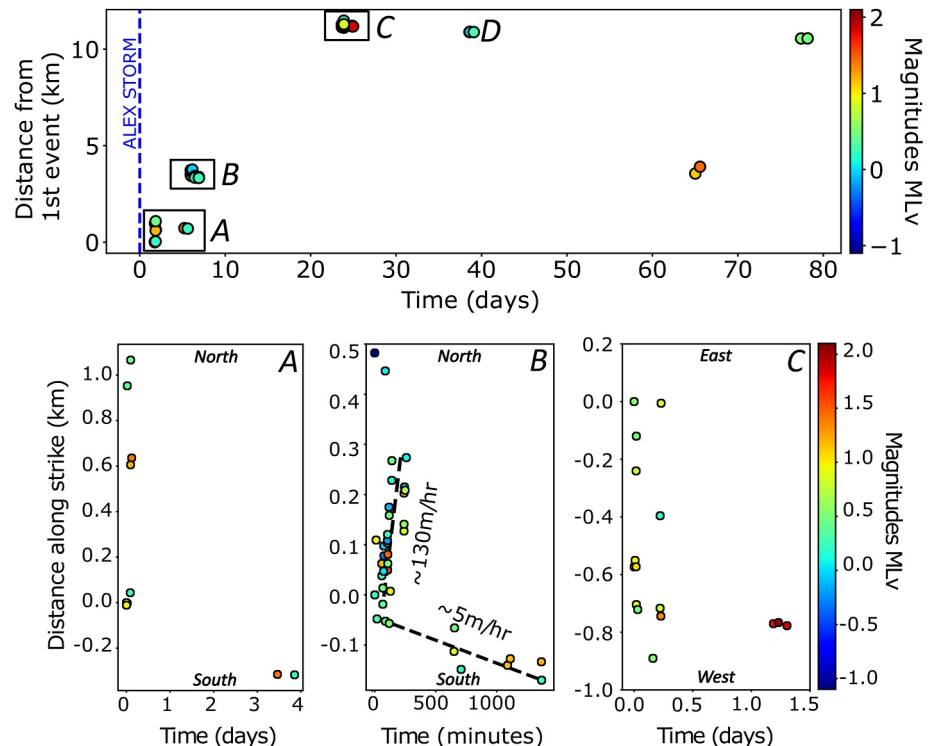


**Figure 5.** Migration of the seismicity post the Alex storm relative to the 1st event. Top: Distance-time plot of all the seismic sequences. (Bottom) Oriented close-up view on each individual swarm labeled A, B and C.

The bottom subplots in Figure 5 are presented as distance-time plots along the strike. In this context, strike is defined as the general horizontal direction of each swarm. These plots serve to emphasize any potential migration of the seismicity. Upon closer examination, the A and C swarms, comprising 10 and 20 events, respectively, do not show any clear migration patterns. For swarm A, a rapid northward migration ( $\sim 340$  m/hr) might be estimated with the first 8 earthquakes, but the small number of earthquakes prevents reliable interpretation. Similarly, for swarm C, the rapid apparent westward migration of  $\sim 150$  m/hr could be an over-interpretation of the results due to the small number of earthquakes.

A robust analysis can be conducted with swarm B, which consists of 42 located events. A bidirectional migration is clearly depicted in subplot B of Figure 5. In the first  $\sim 300$  min, the seismicity migrates northward at the velocity of  $\sim 130$  m/hr. Following this, a second migration with a slower southward velocity ( $\sim 5$  m/hr) becomes evident as the seismicity is mainly activated south of the area of seismic initiation.

The velocities observed within this swarm can be linked to classical physical mechanisms governing seismicity propagation. Velocities below 100 m/hr are compatible with the mechanism of fluid-diffusion (Chen et al., 2012), while velocities ranging from 100 to 1,000 m/hr are more in line with the aseismic slip mechanism (Roland & McGuire, 2009). In the case of swarm B, the bidirectional migration is noteworthy, where northward migration could be indicative of aseismic slip, while the southward migration aligns with fluid-diffusion process.

This swarm is a good illustration of the potential interaction between multiple processes that initiate and sustain seismicity. In areas characterized by low deformation rates, transient processes can be more easily identified, as their associated deformations are not overshadowed by more pronounced tectonic deformations. The observed interaction between fluid diffusion and aseismic slip are consistent with findings from prior studies (Cappa et al., 2019; De Barros et al., 2020).

## 6. Modeling the Seismicity Evolution

The seismic observations following the 2020 Alex storm present a unique opportunity to investigate the intricate interplay between rainfall infiltration and swarm mechanics. This section delves into modeling results to explore the underlying processes driving the swarm and assess the relative contributions of extreme rainfall, fluid pressure diffusion from water infiltration, and intermittent stress perturbation from slow aseismic slip in driving the seismicity. We first outline the modeling strategy employed to calculate fluid pressure and stress changes associated with rainfall, and the link with changes in seismicity rates. Next, we model the temporal evolution of seismicity during the swarm sequence by comparing (a) a fluid-driven model and (b) a stress-driven model based on rate-and-state friction formalism. We then discuss the disparities between the two models and explain how they provide insights into the stress perturbations associated with slow aseismic slip. These perturbations, in turn, contribute to sustaining the swarm activity over the 100 days following the storm.

### 6.1. From Rainfall to Fluid Pressure and Stress Changes

In the Earth's crust, faults in intraplate regions are generally considered in a critically stressed state (Townend & Zoback, 2000). Consequently, small changes in fault loading conditions can trigger earthquakes that release energy stored as tectonic strain. For instance, it has been shown that fluid pressure changes as low as 0.5 kPa and stress changes as low as 0.07 kPa are sufficient for earthquake triggering (Wilson et al., 2022).

Here, to quantify the effects of rainfall on fault activation at the seismic nucleation depth, we calculated the stress changes in response to time-varying surface loads using the Coulomb's theory in which the Coulomb stress change ( $\Delta\text{CFS}$ ) is defined as (Jaeger et al., 2007):

$$\Delta\text{CFS} = \Delta\tau + \mu\Delta\sigma_n + \mu\Delta P \quad (2)$$

where the symbol  $\Delta$  denotes a change,  $\tau$  is the shear stress on the fault (positive when increased in the direction of fault slip),  $\sigma_n$  is the total normal stress on the fault (positive for extension, i.e., when the fault is unclamped),  $\mu$  is the friction coefficient of the fault, and  $P$  is the fluid pressure in the fault. A positive Coulomb stress change will promote fault rupture, potentially seismic; conversely, a negative Coulomb stress change will tend to lock the fault.  $\Delta\tau$  and  $\mu\Delta\sigma_n$  in Equation 2 denote the contribution of mechanical stressing, while  $\mu\Delta P$  is the direct hydraulic contribution of the change in fluid pressure on the fault (positive indicates a pressure increase). Thus, fault

slip may be induced by an increase in shear stress or fluid pressure, or by a reduction in normal stress or friction coefficient.

The fluid pressure change ( $\Delta P$ ) develops in two ways (Chen & Talwani, 2001; Talwani, 1997). First, an instantaneous response occurs to undrained loading ( $\Delta P_u$ ) caused by the compression of the porous rock associated with the weight of the water mass at the ground surface. Second, the diffusion of fluid pressure ( $\Delta P_d$ ) from the ground surface to the hypocentral location. So, the fluid pressure change ( $\Delta P$ ) is defined as follows:

$$\Delta P = \Delta P_u + \Delta P_d \quad (3)$$

The instantaneous increase of fluid pressure ( $\Delta P_u$ ) due to undrained effect (Skempton, 1954) is expressed as:

$$\Delta P_u = B\bar{\sigma} \quad (4)$$

where  $B$  is the Skempton's coefficient and the average change in the mean stress is:

$$\bar{\sigma} = \frac{(\sigma_{xx} + \sigma_{yy} + \sigma_{zz})}{3} \quad (5)$$

For a uniform circular load, the mean stress can be calculated from the vertical, radial and transverse horizontal stresses estimated at depth ( $z$ ) and distance ( $r$ ) from the water mass at the ground surface as follows (Dura-Gomez & Talwani, 2010; Liu et al., 2011):

$$\sigma_z = -\frac{3Fz^3}{2\pi r^5} \quad (6)$$

$$\sigma_r = \frac{F}{2\pi} \left[ \frac{(1-2\nu)}{R^2} \left(1 - \frac{z}{r}\right) - \frac{(3R^2z)}{r^5} \right] \quad (7)$$

$$\sigma_t = \frac{F}{2\pi} (1-2\nu) \left( -\frac{1}{R^2} + \frac{z}{Rr} + \frac{z}{r^3} \right) \quad (8)$$

where  $F$  is the concentrated force at the origin,  $F = \rho ghA$ ,  $h$  is the height of the water column,  $A$  is the surface area of the water mass,  $g$  is the acceleration of gravity ( $m/s^2$ ), and  $\rho$  is water density ( $kg/m^3$ ).  $\nu$  corresponds to the Poisson ratio. The distance  $r$  is defined as  $r = \sqrt{x^2 + y^2 + z^2}$  and its horizontal projection  $R$  is defined as  $R = \sqrt{x^2 + y^2}$ .

For the fluid diffusion process ( $\Delta P_d$ ), we assume that the change in groundwater level ( $\Delta W$ ) associated with rainfall rate ( $Q$ ) is coupled with the poroelastic response of the fluid saturated crust. Thus, the variations of groundwater level depend on the rainfall history (Figure 6a) and the hydraulic properties of the rock formations. Here, we consider a simple model where the groundwater level change is equal to the deviation of the rainfall from the average precipitation rate (Hainzl et al., 2006, 2013). The groundwater load change over time can be numerically considered as a succession of load changes caused by rainfall. Based on the estimated changes of the groundwater level, we can calculate the fluid pressure changes at depth ( $z$ ) assuming a 1-D diffusion process in a porous medium (Miller, 2008). The solution of the 1-D diffusion equation (Hainzl et al., 2013; Roeloffs, 1988; Simpson, 2001) is given by:

$$\Delta P_d(z,t) = \left[ (1-\alpha) \operatorname{erfc} \left( \frac{z}{\sqrt{4Dt}} \right) + \alpha \right] \rho g \Delta W \quad (9)$$

where  $t$  is the time (s),  $g$  is the acceleration of gravity ( $m/s^2$ ),  $\alpha$  is a model parameter related to the Skempton coefficient ( $B$ ) and the Poisson ratio ( $\nu$ ) as  $\alpha = B(1+\nu)/[3(1-\nu)]$ ,  $\rho$  is water density ( $kg/m^3$ ),  $\operatorname{erfc}$  is the complementary error function, and  $D$  is the hydraulic diffusivity ( $m^2$ ). When the undrained effect is dominant,  $\alpha$  tends to one, while, when the drained effect is dominant,  $\alpha$  tends to zero (Dura-Gomez & Talwani, 2010). By convolution of the groundwater level changes with Equation 9, the fluid pressure change at depth is calculated in response to the measure surface rainfall. Here, we ignore the hydromechanical effect of stress-dependent

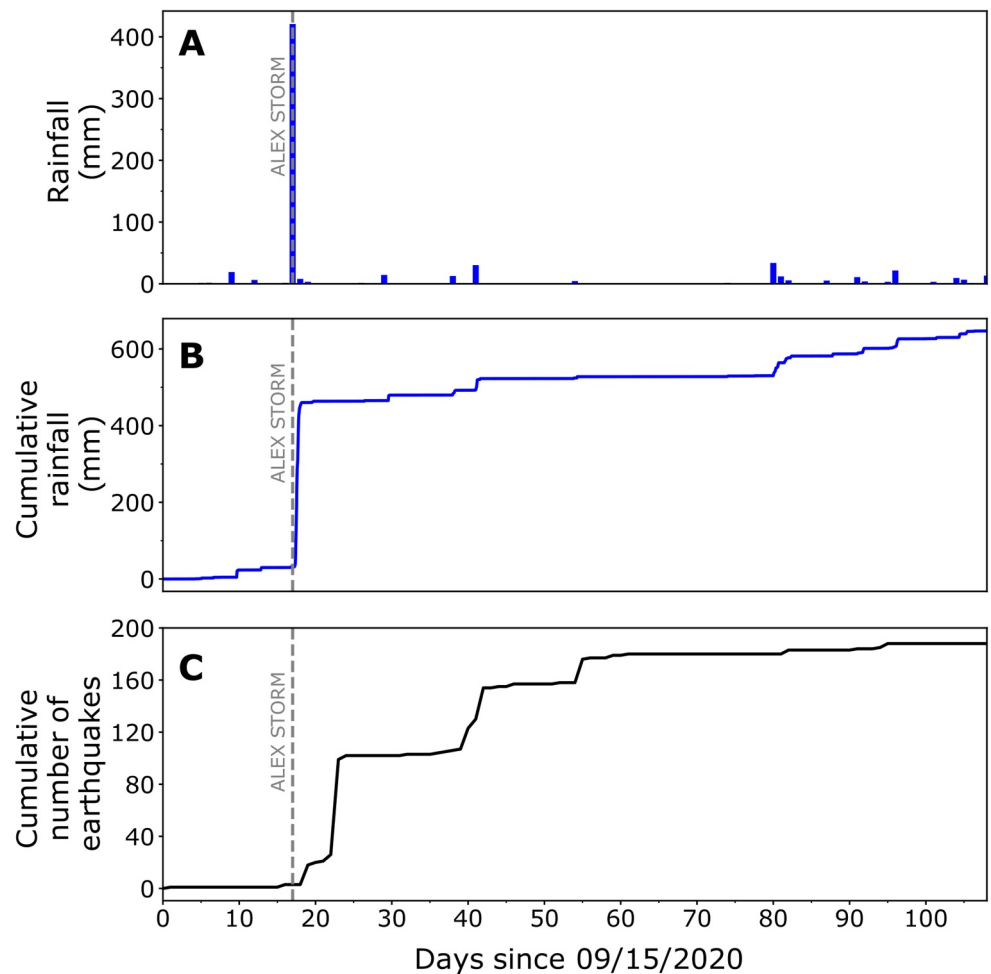


**Figure 6.** Time series of (a) daily and (b) cumulative rainfall, as well as (c) cumulated number of earthquakes. The gray vertical line indicates the time window of the 2020 Alex storm. Rainfall is measured at the Clans station located in the seismically active area (see Figure 1).

hydraulic diffusivity due to the inherent difficulties to constrain the distribution of rock and fault properties at depth, and focus on the direct effects of fluid pressure changes. The interaction between rainfall and seismicity was previously studied with similar models for the fluid pressure changes (Hainzl et al., 2006, 2013; Miller, 2008). The tested values of these parameters are listed within Table 1. Here, we have tested a classic range of hydraulic diffusivities, from 0.1 to 10 m<sup>2</sup>/s (e.g., De Barros et al., 2021), for the porous and permeable sandstone and limestone layers observed in the studied area. The fluid pressure change was calculated from the ground surface to a depth of 6 km, a depth below the location of observed seismicity to avoid numerical boundary effects.

**Table 1**  
Model Parameters Used to Calculate Change in Fluid Pressure and Coulomb Stress

Properties	Value
Skempton coefficient (B)	0.5
Poisson ratio ( $\nu$ )	0.31
Hydraulic diffusivity (D)	0.1, 1, 5, 10 m <sup>2</sup> /s
Effective friction coefficient ( $\mu$ )	0.3, 0.4, 0.5, 0.6
Water density ( $\rho$ )	1,000 kg/m <sup>3</sup>

## 6.2. From Stress Changes to Seismicity Rate Changes

Subsequently, we relate the change in Coulomb stress ( $\Delta\text{CFS}$ ) to the time-dependent seismicity rate change ( $dR/dt$ ) using Dieterich's seismicity rate theory (Dieterich, 1994). We employed this approach for the two tested models. First, we conducted a fluid-driven model for rainfall-induced fluid pressure, and second, a stress-driven model for stress perturbations due to aseismic slip transient.

The Coulomb stressing rate ( $\dot{\tau}$ , time derivative of the Coulomb stress changes defined in Equation 2) is used as input to the rate-and-state seismicity theory originally proposed by Dieterich (1994), and then adapted by Segall and

Lu (2015) and Heimisson and Segall (2018), to derive the evolution of seismicity rate. The seismicity rate is calculated as:

$$\frac{dR}{dt} = \frac{R}{t_a} \left( \frac{\dot{\tau}}{\dot{\tau}_0} - R \right) \quad (10)$$

where  $R$  is the relative seismicity rate (i.e., the seismicity rate divided by the background seismicity rate  $r_0$  associated with tectonic loading),  $\dot{\tau}_0$  is the background stressing rate, and  $t_a$  is a characteristic time decay which depends on a dimensionless fault parameter “ $a$ ” (which quantifies the direct effect of rate-and-state friction behavior of the fault) and the temporal evolution of normal effective stress  $\sigma'_n$  (i.e., total normal stress minus fluid pressure):

$$t_a = \frac{a\sigma'_n}{\dot{\tau}_0} \quad (11)$$

This model of seismicity rate is the simplest equation that both admits a steady state solution and also predicts Omori-like decay following a rapid change in stress (Segall & Lu, 2015). A limitation of the model is that it does not account for stressing due to interactions between earthquake sources.

The ordinary differential Equation 10 is solved using an explicit fifth-order Runge-Kutta algorithm with adaptive time step (Fehlberg, 1969). The relative error tolerance is  $10^{-6}$  and the absolute tolerance is set to a very small value so that error control is essentially only relative.

For the stress-driven model testing the effects of stress perturbations due to aseismic slip transient, we approximate the stressing rate history with a series of seven pulse functions inferred from the seven main bursts of seismicity visible on Figures 2c and 2d. This assumption is supported by previous studies indicating the imbricated occurrence of intermittent discrete seismic ruptures of various amplitudes in a slowly slipping fault (Lengliné et al., 2017). Before the onset of stress pulse, the background stressing rate is  $\dot{\tau}_0$ . During a seismic burst, the stressing rate increases to  $\dot{\tau}$ ; then, it returns to background. A single pulse is modeled with the Gumbel function:

$$F = \omega \frac{\exp(-z) z}{\beta}, \quad z = \exp\left(\frac{-t - t_p}{\beta}\right) \quad (12)$$

where  $\omega$  is an amplification factor of the pulse,  $\beta$  is a parameter controlling the pulse width,  $t$  is the time, and  $t_p$  is the starting time of the pulse.

### 6.3. Inversion Procedure

The stress-driven model based on stress perturbations due to aseismic slip is governed by 24 parameters ( $r_0$ ,  $t_a$ , and  $\dot{\tau}_0$  in Equation 10, plus seven times  $\omega$ ,  $t_p$  and  $\beta$  in Equation 12). In order to simplify the model, the values of  $\beta$  and  $t_p$  are fixed relative to the duration of each seismic burst (Figures 2c and 2d). The background seismicity rate  $r_0$  is estimated from the regional catalog before and after the seismic sequence associated with the Alex storm and is set to 3 events per month. Then, the values of the 9 others free parameters are determined by solving an inverse problem consisting in finding the optimal values that provide a theoretical cumulative number of earthquakes (i.e., integration of  $dR/dt$ ) best explaining the data. This approach was already used in previous studies (e.g., Heimisson & Segall, 2020; Luu et al., 2022; Segall et al., 2006). It offers a larger data set for comparison with numerical models than relying solely on daily earthquake counts for the seismicity rate.

This inverse problem is solved for 5 million of explored solutions using a simulated annealing algorithm (Kirkpatrick et al., 1983). This algorithm is designed to make an efficient random exploration of the solution space. Exploration consists in seeking the optimal solution corresponding to the absolute minimum of misfit function while avoiding solutions of local minima. In the initial steps, solution space is broadly explored and then in later iterations, exploration focuses on regions that fit the data well. The concept of the algorithm hinges on distinctive feature associated with temperature variation, a key aspect integrated into the characteristics of the algorithm. This entails a systematic reduction of the temperature as the inversion progresses. The algorithm starts

initially with a high temperature and gradually decreases it at each step according to a predefined annealing schedule. In our investigation, we explored three distinct schemes for the temperature evolution: (a) a linear decrease from the highest to the lowest temperature, along with a cyclic reduction and increase of temperature from the highest to the lowest value considering (b) the current solution of the present cycle as the initial solution for the next cycle, or (c) the best-fit solution of the present cycle as the initial solution for the next cycle. This approach yields an ensemble of best-fit solutions for various conventional annealing schedules.

Following this, the inversion procedure was performed for different random sets of initial values for the nine parameters. The bounds on the prior distribution are given by  $10^{-6} < \tau_0 < 10^{-3}$  MPa/day,  $1 < t_a < 30$  days, and  $0.01 < \omega < 0.2$ . The misfit between the observations and predictions is estimated with the reduced chi-square ( $\chi_r^2$ ):

$$\chi_r^2 = \frac{1}{N} \sum_{i=1, N} \left( \frac{\text{obs}_i - \text{pred}_i}{\sigma_i} \right)^2 \quad (13)$$

where  $N$  is the number of observations (i.e., 188) minus the number of free model parameters (i.e., 9), and  $\sigma_i$  is the uncertainties (here, we consider 1% for measurement and model).

To assess the sensitivity of the best-fit numerical solution to the data, we ran the inversion 30 times, with 10 runs conducted for each of the three annealing schedules mentioned above. By doing so, the dispersion of the 30 solutions gives an estimation of the uncertainties for each free model parameters.

## 6.4. Modeling Results

### 6.4.1. Can Seismicity Be Explained by Stress Changes Induced by an Increase in Fluid Pressure?

It is commonly assumed that heavy rainfall can potentially induce seismicity through two types of mechanisms (Miller, 2008; Perrochet et al., 2023): (a) the accumulation of substantial water mass in the subsurface above critically stressed faults, leading to stress variations large enough to trigger a seismic ruptures, or (b) the diffusion of a front of pressurized fluids from surface to seismogenic depth, resulting in a reduction of normal effective stress and resistance on faults, sufficient to initiate ruptures. In the case of the 2020 Alex storm, a linear correlation between the seismicity and rainfall using a 1-day sliding window (Figure S8 in Supporting Information S1) indicates a 6-day time delay between them, highlighting a potential contribution of fluid pressure and associated poroelastic effects in triggering and driving the seismicity. We investigate these two mechanisms in the following sub-sections.

#### 6.4.1.1. Impact of Surface Flooding Loading at the Depth of Observed Seismicity

Here, we examine how a massive weight of fluids can perturb the stress on a fault at the depth of observed seismicity. In the seismic zone, the subvertical fault (80°) is experiencing only slight effects of vertical loads. The Tinée valley lacks karstic environment dominated by high transmissive hydraulic conduits, a condition favorable to the fluid mass gathering (D'Agostino et al., 2018; Derode et al., 2023; Perrochet et al., 2023). Thus, the Tinée river bed collects most of the surface runoff. However, the flash floods induced by the storm also triggered numerous landslides and destruction, resulting in a substantial mass of mixed water and sediments carried through the valley. We estimated the area of flood to be 3.5–7 km long, 40 m wide, and 4–10 m high by analyzing IGN (National Institut for Geographic and Forestry Information) satellite images before and after the storm, combined with the local geometry of the valley. Thus, the volume of the water mass is comprised between  $5.6 \times 10^5$  and  $2.8 \times 10^6$  m<sup>3</sup>. The flood density was estimated between the classical value of  $\rho = 1,200$  kg/m<sup>3</sup> for water body slightly concentrated into unconsolidated sediments (silts, sand, etc.), and  $\rho = 2,650$  kg/m<sup>3</sup>, equivalent to sediment density (Dietze et al., 2022). The high  $\rho$  value, compared to the usual value for water, reflects the large volumes of rocks, sediments and rubbles transported by the torrent, aiming to estimate the maximum possible loading perturbation to analyze its impact at the seismogenic depth.

Equations 6–8 were used to estimate the vertical, transverse and radial stresses at the depth of seismicity, considering the distance between the surface loading and the seismicity. To better constrain the model, we calculated two cases: (a) the centroid of the flood mass is located in the mid-length of the flood, in the river bed (around La Condamine village, between swarm A and swarm B in Figure 3), and the seismogenic fault is at the location of the swarm B; (b) the centroid of the flood mass is located right above the seismogenic fault.



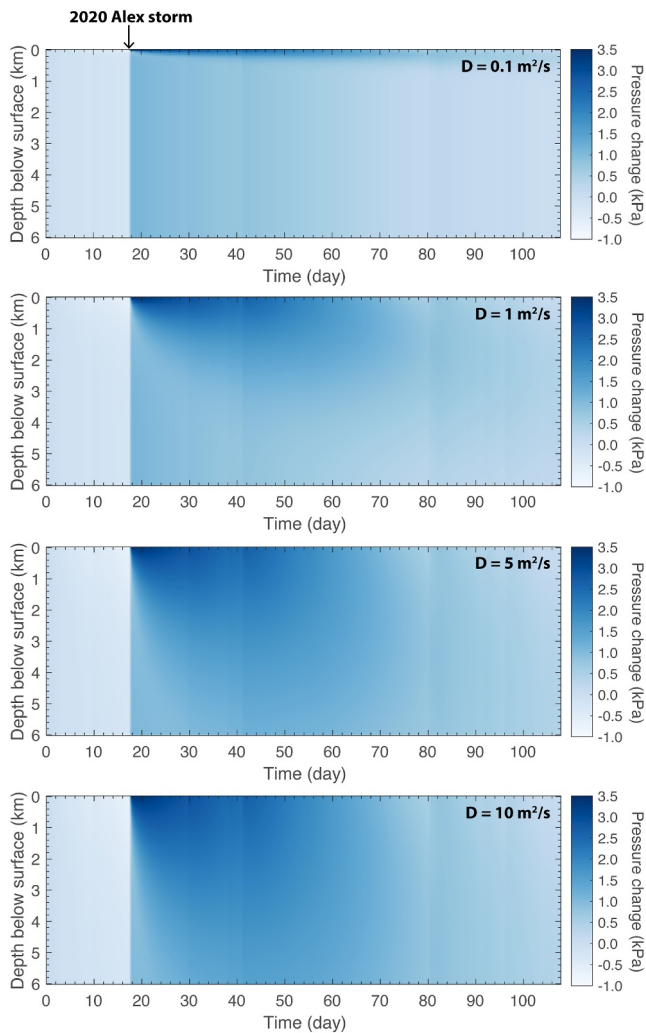


**Figure 7.** Fluid pressure change induced by the rainfall history (daily data) for different values of hydraulic diffusivity (0.1, 1, 5, 10 m<sup>2</sup>/s).

In the most realistic scenario (case 1), the mean stress varies from 64 to 708 Pa at 4-km depth, and the undrained pressure ranges from 32 to 354 Pa. In the worst-case scenario (case 2), the mean stress ranges from 115 to 1,268 Pa at the same depth, with the undrained pressure estimated at 57–634 Pa. In comparison, as a point of reference, an overpressure of 8 MPa (approximately 8,000 times higher than the magnitude of perturbation in this study), resulting from an abrupt vertical loading of a water column due to intense rainfall in the Nîmes fault region in September 2002 triggered 80 earthquakes (Rigo et al., 2008).

Based on the above calculations, the pressure change induced by the undrained response at the depth of the seismic zone is only on the order of hundreds of Pascals, representing a very low stress perturbation in the geological medium. Moreover, the undrained fluid pressure is the largest at the time of the flood, and gradually decrease with time. Thus, the impact of the instantaneous load associated with the temporary storage of a heavy water mass at the ground surface on the seismicity is rather weak, leading to a very low triggering ability. In this case, a massive loading due to the extreme flooding cannot be considered as the main or only mechanism responsible for the increased seismicity rate.

#### 6.4.1.2. Seismicity Evolution From a Fluid-Driven Model

Figure 7 presents the migration of fluid pressure from the surface owing to rainfall through the permeable medium until 6 km depth. In all modeled scenarios, the fluid pressure diffusion is calculated over a period of 108 days, starting from 15 September 2020, about 18 days before the Alex storm to avoid boundary effects. Modeling results show that rainfall can induce fluid pressure changes on the order of kilopascals at depths of few kilometers for a range of hydraulic diffusivity comprised between 0.1 and 10 m<sup>2</sup>/s (Figure 7). At depths between 3 and 4 km below the surface where seismicity occurs, the increase in fluid pressure varies from 0.9 to 2 kPa, respectively, for the lowest and highest values of hydraulic diffusivity (Figures 8a and 8b). At the peak of rainfall, results indicate a sudden and rapid pressure increase up to 0.9 and 1.1 kPa, depending on diffusivity. Then, the pressure continues to slowly increase during 23 days after the storm, and then decreases, for the highest diffusivities (5 and 10 m<sup>2</sup>/s), while pressure decreases slowly immediately

after the storm for the lowest diffusivities (0.1 and 1 m<sup>2</sup>/s). The small intermittent pressure increases observed at distinct times depicts the response to local rainfall (Figure 8).

From the pressure variations, the maximum changes in Coulomb failure stress ( $\Delta$ CFS) are comprised between 0.7 and 0.8 kPa for the highest diffusivity, at 3 and 4 km depth, respectively. By varying the friction coefficient (Figures 9a and 9b), the maximum stress changes vary between 1 and 1.4 kPa.

Using our estimated values of Coulomb stress changes induced by fluid pressure diffusion due to rainfall, the calculated cumulative number of earthquakes is less than 4 for different tested values of background stressing rate ( $\tau_0$  from 1 to 10 kPa/yr) and characteristic time decay ( $t_a$  from 5 to 30 days), in a range of values representative of natural conditions in the studied area (Figures 9c and 9d). This cumulative number of seismic events is much lower than the 185 earthquakes observed after the Alex storm (Section 5). This result shows that the stress changes associated with rainfall infiltration and fluid pressure diffusion is rather weak, so their triggering ability is insufficient to explain the data.

We conclude that another mechanism is at play to produce the stress perturbations capable of triggering the observed swarms.

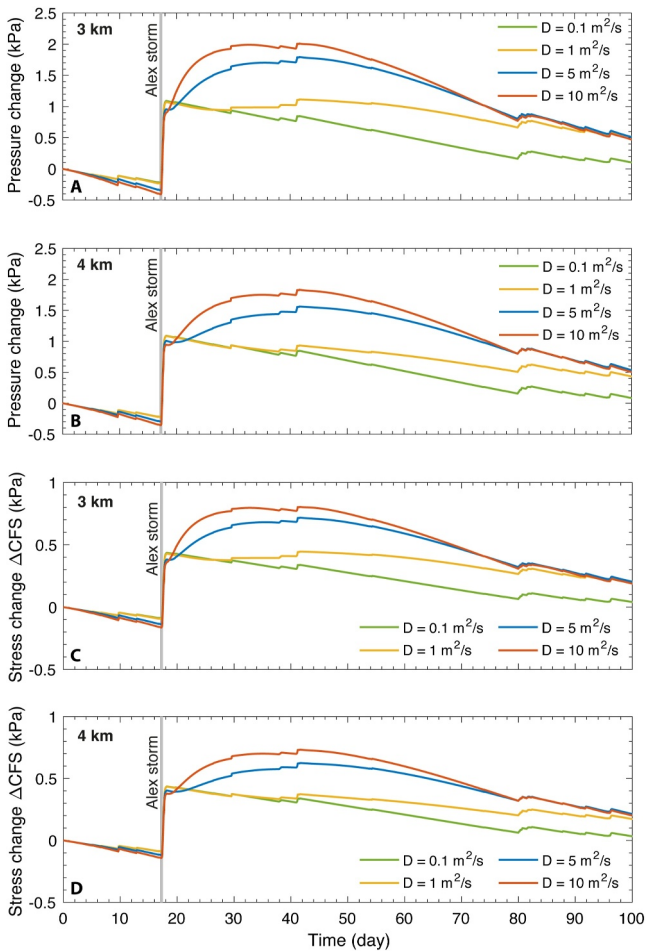


**Figure 8.** (a and b) Fluid pressure and (c and d) Coulomb stress changes due to rainfall for a variety of hydraulic diffusivity ( $0.1, 1, 5, 10 \text{ m}^2/\text{s}$ ) at different depths (3 and 4 km) in the seismic area. The gray vertical line indicates the time window of the 2020 Alex storm. The effective friction coefficient is taken at 0.4 for calculating the Coulomb stress changes in panels (c) and (d).

#### 6.4.2. Seismicity Evolution From a Stress-Driven Model Associated With Aseismic Slip

In Section 6.4.1, we demonstrated that stress changes resulting from fluid pressure diffusion cannot explain the observed seismicity. Additionally, the envelope of seismicity rate (Figure 2d) appears to decrease exponentially, consistent with a relaxation process (Hainzl & Christophersen, 2017) following the Alex Storm. We initially tested this assumption and found that a basic relaxation model only partially reproduces the observed seismicity rate (Text S4, Figure S9 in Supporting Information S1).

Consequently, we have investigated a more complex model accounting the possibility of stress changes due to aseismic slip migration using a stress-driven model based on Equations 10 and 11 of Dieterich's model, along with Equation 12 for stress loading history. This model introduces an evolving shear stress perturbation, affecting the seismicity rate on a fault. While lacking geodetic observations of a slow slip event in this area to constrain the model, aseismic slip mechanisms have been observed in other regions with earthquake swarms (De Barros et al., 2020; Llenos et al., 2009; Lohman & McGuire, 2007; Sirorattanakul et al., 2022).

Furthermore, in Section 5, we presented evidence that the swarm B, activated 6 days after the storm, exhibits a northward migration whose velocity is consistent with aseismic slip. Consequently, our model assumes that aseismic slip migration serves as the source of intermittent pulses of shear stress perturbation, leading to swarm seismicity. For each seismicity cluster, the amplitudes of each pulse of stress ( $\omega$ ) vary freely in the model, while the duration is fixed based on the data (see Sections 6.2 and 6.3).

Results from 30 inversions show that the model effectively reproduces the observed cumulative number of earthquakes (Figure 10a). Consistent best-fit solutions are obtained for different evolutions of shear stress with final values ranging from  $\sim 206$  to  $\sim 410$  kPa (Figure 10b), corresponding to peaks in stressing rate between 14 and 168 kPa/day. The estimates of model parameters include a relaxation time of  $\sim 16.5$  days ( $\pm 2.4$ ), a background stressing rate of  $\sim 0.057$  kPa/day ( $\pm 0.0084$ ), and  $\sigma_n$  of 0.94 kPa ( $\pm 0.17$ ) (Figure S10 in Supporting Information S1).

The reliability of these results is verified through two additional tests. The first test consists in computing numerical solutions from parameter values that are  $\pm 10\%$  of the maximum and minimum among the 30 best-fit parameters. The resulting numerical solutions (Figure S11 in Supporting Information S1) do not align with the observed seismic data, which clearly reinforces confidence in the original best-fit solution. The second test is a comparative analysis between the inversion of the cumulative number of earthquake and the maximum log-likelihood approach, a common method for fitting models with earthquake data (e.g., Hainzl et al., 2006; Hardebeck, 2012; Zhuang et al., 2012). The results show that both approaches yield similar solutions (Figure S12 in Supporting Information S1), further validating the accuracy of our model.

In addition, we have set the prior distribution of the relaxation time ( $t_a$ ) between 1 and 30 days, a reasonable assumption considering the short duration of observed seismic bursts, which typically range between 1 and 6 days (Figures 2 and 6c). However, these values are shorter than those generally observed for aftershocks sequences, which can last from several months to years or even decades (Hainzl et al., 2016; Utsu et al., 1995). To account for this, we have tested a new inversion with a larger prior distribution of the relaxation time, extending it to 360 days. We found a best-fit solution (Figure S13 in Supporting Information S1) with a  $t_a$  of 22.27 days, a value in agreement with the previously calculated range ( $12.12 < t_a < 22.02$  days) for the 30 best-fit solutions (Figure S10 in Supporting Information S1). Thus, a larger prior distribution of  $t_a$  has a limited impact on the best-fit numerical solution.

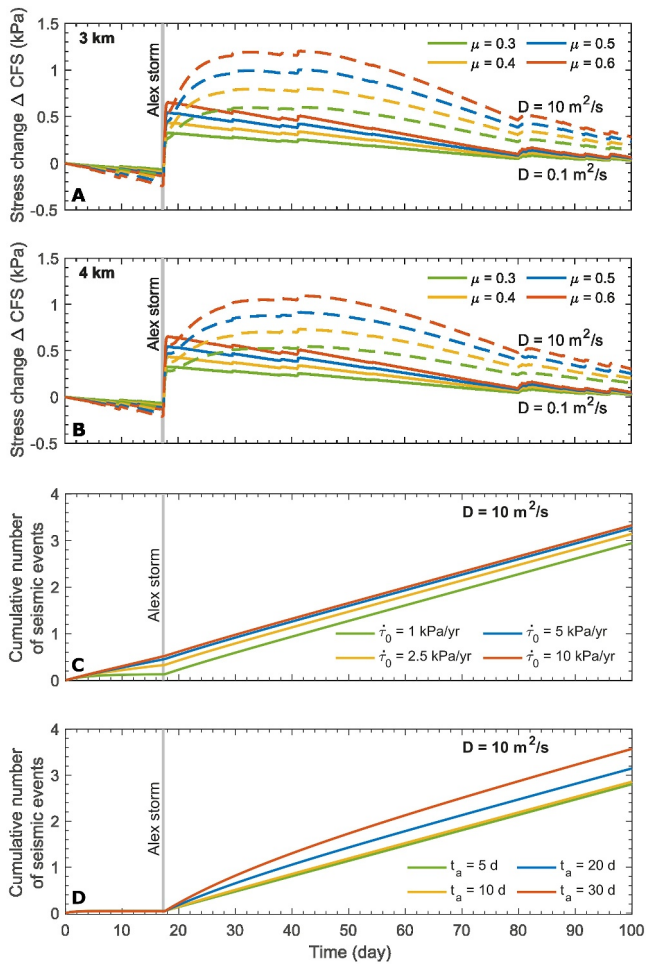


**Figure 9.** Sensitivity of (a) and (b) the stress change at depths of 3 and 4 km to the friction coefficient, assuming two cases of hydraulic diffusivity (0.1 and  $10 \text{ m}^2/\text{s}$ ), and cumulative number of earthquakes to (c) tectonic stressing rate ( $\dot{\tau}_0$ ) and (d) the relaxation time ( $t_a$ ) in response to fluid diffusion due to rainfall considering a hydraulic diffusivity of  $10 \text{ m}^2/\text{s}$ .

The obtained value of background stressing rate ( $\dot{\tau}_0 = 20.52 \text{ kPa/yr}$ ) is consistent with a long-term stressing rate of  $30 \text{ kPa/yr}$  estimated in this region assuming a maximum strain rate of 1 micro-strain per year (Calais et al., 2002; Eva et al., 2020; Larroque et al., 2009; Nocquet, 2012) and a rock shear modulus of  $30 \text{ GPa}$ .

While the estimated value of parameter  $a\sigma_n$  at  $0.94 \text{ kPa}$  is relatively small, similar values have been estimated for various tectonic settings based on the seismicity response to transient stressing. For example, Sirorattanukul et al. (2022) reported a range of  $0.4\text{--}1.2 \text{ kPa}$  for the 2020 Westmorland, California earthquake swarm. Hainzl et al. (2006) found a value of  $0.11 \text{ kPa}$  for a rainfall-triggered earthquake swarm at Mt. Hochstaufen in Germany. Rinaldi et al. (2020) calculated  $a\sigma_n$  of  $0.8 \text{ kPa}$  for reservoir-induced seismicity at Val d'Agri in Italy. These small values of  $a\sigma_n$  suggest the likelihood of very high fluid pressure, or faults with a very small rate-and-state parameter ( $a$ ), or a combination of both, in a mechanically weak source region at the depths of observed seismicity in our study. For example, for the swarm triggered 6 days after the storm, if we assume the overburden normal stress at  $3.6 \text{ km}$  ( $\sigma_n \sim 108 \text{ MPa}$ ) and a typical lower bound value of parameter  $a \sim 0.001$  from laboratory experiments (Marone, 1998), a value of  $a\sigma_n$  of  $108 \text{ kPa}$  is expected. This value is  $\sim 115$  times greater than those derived from the inversion of the best-fit numerical solutions to seismicity data. Conversely, if we assume  $\sigma_n$  to be  $108 \text{ MPa}$ , we would need a very small value of parameter “ $a$ ” of approximately  $8.7 \times 10^{-6}$  to align with our estimated value of  $a\sigma_n$ . This analysis shows the presence of weak faults at the depth of seismicity. These faults are likely under critical stress conditions and near the point of failure.

## 7. Discussion

### 7.1. Distribution of the Seismicity Relative to the Geological Conditions

The depth of seismic swarms, and the likelihood that they were triggered by slow aseismic slip, constrain the depth of the slow slip. On the geological map (Figure 1) of the lower Tinée valley, the meso-Cenozoic sedimentary cover is discernible, distinctly separated from the underlying basement (comprising Permian pelites and migmatites) by a Triassic layer. Based on field data (Faure-Muret, 1957), two lithostratigraphic logs (see Figure S14 in Supporting Information S1) provide contrasting estimations for the thickness of geological layers in this region—one representing the minimum thickness, and the other the maximum. The mean vertical location uncertainty provided by NonLinLoc (phase of the Sismoazur data set relocation, Section 4.3) is around  $900 \text{ m}$ . Hence, considering the two possible distributions of lithology and the vertical uncertainty location of seismicity, earthquakes occurred either within the crystalline basement or in proximity to the interface between the crystalline basement and the Permian fractured layer. In light of the dip of the layers and the geological map, the former scenario, wherein seismic ruptures occur within the crystalline basement, remains more plausible and consistent with the available data.

The crystalline basement outcrops north of Tinée valley (massif of the Argentera-Mercantour). This igneous and metamorphic massif, originating from the Variscan period, was exhumed at the end of the Alpine orogenesis within a transpressional regime that reactivated large NW-SE strike-slip faults (Bigot-Cormier et al., 2006). Consequently, the crystalline basement lying  $3\text{--}4 \text{ km}$  beneath the Tinée valley is likely heterogeneous with a fault system of variable hydraulic and frictional properties. As a result, this geological context renders the crystalline basement susceptible to hosting a portion of the seismicity observed in the region. Conversely, faults in the sedimentary cover primarily slip aseismically.

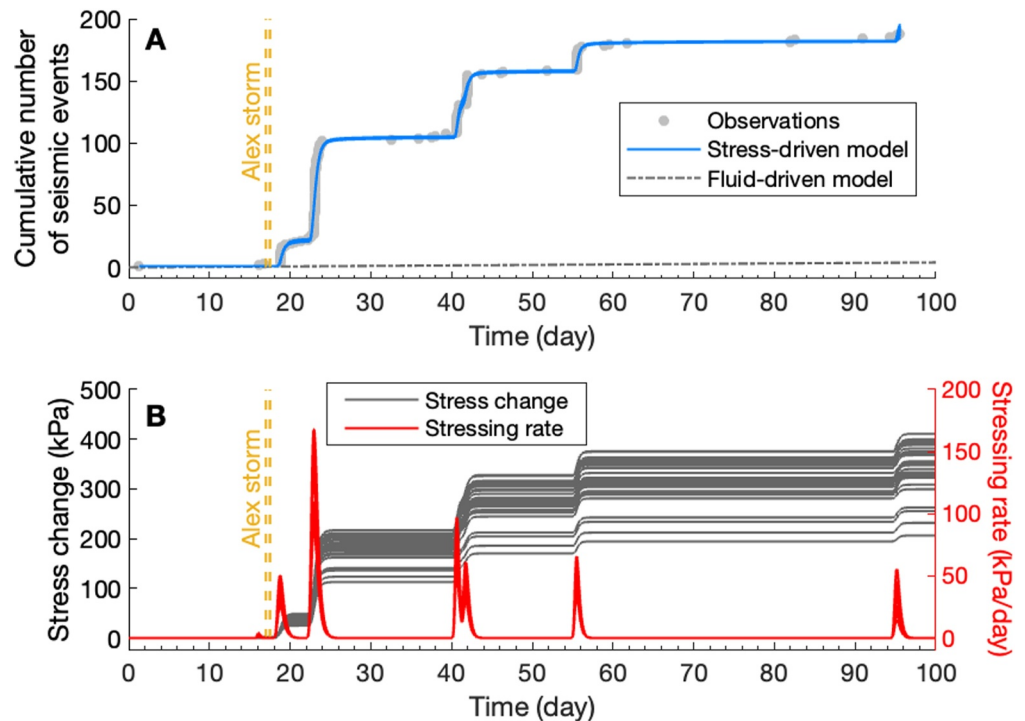


**Figure 10.** Cumulative number of earthquakes detected compared to that predicted for a stressing rate history associated with a slow slip event. (a) Observed earthquakes count in daily bins (gray dots) and the 30 best-fit predicted solutions (blue lines). Vertical orange dashed lines mark the beginning and end of the Alex storm. (b) Inverted stressing rate history estimated from the sum of individual pulses, using the Gumbel function (Equation 12), and stress changes used to derive the predicted seismicity.

## 7.2. Mechanisms Involved in the Triggering Sequence of Seismic Swarms and Correlation With Rainfall

Through our investigations, we show that the earthquake swarms following the 2020 Alex storm can be explained by a series of intermittent shear stress perturbations with magnitudes largely greater than ones produced by fluid pressure diffusion due to rainfall ( $\sim 294$  times the low bound of  $\Delta CFS$  at 0.7 kPa, and 292 times the upper bound of  $\Delta CFS$  at 1.4 kPa). The contribution of a slow aseismic slip is consistent with the migration velocity ( $\sim 130$  m/hr) of earthquakes northward within the swarm B (Section 5.3). While the fluid-driven model indicated that the contribution of fluid pressure changes is limited at the depth of seismicity, the diffusion of a pressure front from the ground surface could participate in the initiation or acceleration of an aseismic slip on faults critically stressed. Then, the slow slip event produces sufficient stress changes to trigger earthquakes along the main fault zone. Our model is consistent with recent results, which showed that natural fluid intrusion can induce aseismic slip on faults (Yukutake et al., 2022). Subsequently, seismicity migration reflects the aseismic slip propagation.

Additionally, we conducted a theoretical analysis (refer to Text S5 in Supporting Information S1), estimating slip velocities ranging from 0.1 to  $12 \times 10^{-6}$  m/s (Figure S15a in Supporting Information S1). This estimation is based on the observed rupture propagation velocity during seismic bursts (ranging from 5 to 130 m/hr; see Figure 5) and reasonable stress drops (Gao et al., 2012) within the range of 0.1–10 MPa (Text S5 and Figure S15a in Supporting Information S1). The calculated slip velocities align with previous analyses of seismic swarms driven by aseismic creep (Lohman & McGuire, 2007; Roland & McGuire, 2009). Once aseismic slip initiates, it has the potential to escalate, influencing stress on small asperities with critical earthquake nucleation lengths ranging from 0.1 to 5.48 m (Figure S15b in Supporting Information S1). The intermittent stress perturbations, as indicated by our modeling, may trigger seismic activation of slip on these asperities, resulting in earthquakes that manifest as minor swarms. This sequential progression aligns with findings from observations on natural faults (De Barros et al., 2020; Lengliné et al., 2017), and theoretical models (Bhattacharya & Viesca, 2019; Cappa et al., 2019), which demonstrates that the stress perturbation resulting from aseismic slip serves as a trigger for seismic activity.

In the studied area, the absence of geodetic network precludes the measurements of aseismic deformations. Nevertheless, we examined the migration velocity of other swarms within the Tinée valley from 2014 to 2022 (Figures S16–S22 in Supporting Information S1). The spatio-temporal migration of the October 2016 swarm, situated near Marie village (Figure S22 in Supporting Information S1) and characterized by 17 earthquakes, exhibits a northward migration at a rate of  $\sim 4$  km/day, with a corresponding hydraulic diffusivity of  $\sim 1$  m<sup>2</sup>/s. Such values are indicative of seismicity driven by fluid diffusion. The analysis of other historical swarms (Figures S17–S21 in Supporting Information S1) did not reveal aseismic slip velocities that could confirm the presence of aseismic slip as a pervasive background process triggering seismicity in the lower Tinée valley. Nevertheless, a seismic swarm driven by aseismic slip is a reasonable hypothesis in the present case, aligning with observations made in various locations globally (e.g., De Barros et al., 2020; Sirorattanakul et al., 2022; Wei et al., 2015).

Our model results indicated that the increases in fluid pressure due to rainfall vary from 3.5 kPa at shallow depth to a maximum of 2 kPa at the depth of seismicity. This range of pressure changes produce small changes in stress of the order of 1 kPa. Such stress perturbations are in line with trigger stresses caused by solid Earth tides (Scholz et al., 2019) and those required to trigger seismicity on faults (Saar & Manga, 2003). Pressure changes on the order of 10 kPa are conventionally thought to be necessary to initiate mechanical failure and associated geological processes in unstressed media (Costain, 2017). Studies have also shown that stress changes in the range of 0.1–1 kPa are sufficient for rainfall to trigger earthquakes, particularly when the crust is in a critical state (Hainzl et al., 2006). Given the small magnitude of stress perturbation estimated in our study, the source region of seismicity is likely mechanically weak and near the point of failure, requiring only a small amount of stressing to initiate an aseismic slip or accelerating an active slow slip, that then trigger the seismicity.

Triggering of earthquake swarms by aseismic slow slip, alone or in combination with fluid diffusion, was proposed in other regions around the world (e.g., Danré et al., 2022; De Barros et al., 2020; Hatch et al., 2020; Lohman & McGuire, 2007; Roland & McGuire, 2009; Sirorattanakul et al., 2022; Wei et al., 2015; Yoshida & Hasegawa, 2018; Yukutake et al., 2022). Recently, Sirorattanakul et al. (2022) demonstrated the triggering role of a slow slip event starting before the 2020 Westmorland swarm sequence in California. Hatch et al. (2020) also showed that aseismic slip and fluid diffusion are at play in a 10-day swarm sequence near Virginia city, Nevada, in US. Moreover, De Barros et al. (2020) demonstrated that the fluid pressurization in a fault system in the Corinth Gulf in Greece has induced aseismic slip episodes which activate bursts of seismicity during the most intense phases of the swarm.

At the same time, fluid injection experiments into faults (Cappa et al., 2019; De Barros et al., 2018; Guglielmi et al., 2015), reservoir stimulations (Bourouis & Bernard, 2007; Eyre et al., 2019; Wei et al., 2015) and modeling studies (Wynants-Morel et al., 2020) demonstrate the intricate interplay between fluid pressurization, aseismic slip, and seismicity. The increase in fluid pressure can induce the aseismic slip on faults. Then, stress perturbations due to the migration of aseismic slip can trigger seismicity on asperities with rate-weakening frictional properties.

Finally, we propose a model based on a sequence of triggering mechanisms (Figure 11). This sequence initiates with the abrupt and extreme rainfall associated with the Alex storm. Open fault zones facilitate the deep transmission of substantial volumes of rainfall within a critically stressed crust. The stress perturbations resulting from the surface loading coupled with fluid-diffusion and the associated poroelastic response to this meteorological event, may have triggered or accelerated aseismic slip on the extensive N160° faults network below the Tinée valley. Subsequently, the aseismic slip migration increases shear stress on critical asperities, reaching a state favorable to slip seismically. The rupture of these asperities manifests as the swarm seismicity observed in the lower Tinée valley following the extreme rainstorm. The requirement for a critical state might explain why previously activated swarms, such as the one near Marie activated in October 2016 (Figure S22 in Supporting Information S1), were not reactivated following the Alex storm.

### 7.3. Could Other Processes Be Involved in the Triggering of the Swarm Sequence?

There are other possible contributions in the triggering of swarm, including mass displacement, atmospheric loading, tidal interaction or earthquake-earthquake interaction (Foulger et al., 2018; Gao et al., 2000; Hainzl & Ogata, 2005; Métivier et al., 2009). For example, following the 2020 Alex storm, numerous landslides were triggered. The BRGM institute (BDMvt database) documented 134 landslides in the lower Tinée valley, leading to a cumulative destabilized surface area of 322,461 m<sup>2</sup> across approximately 100 km<sup>2</sup> between Saint-Sauveur-

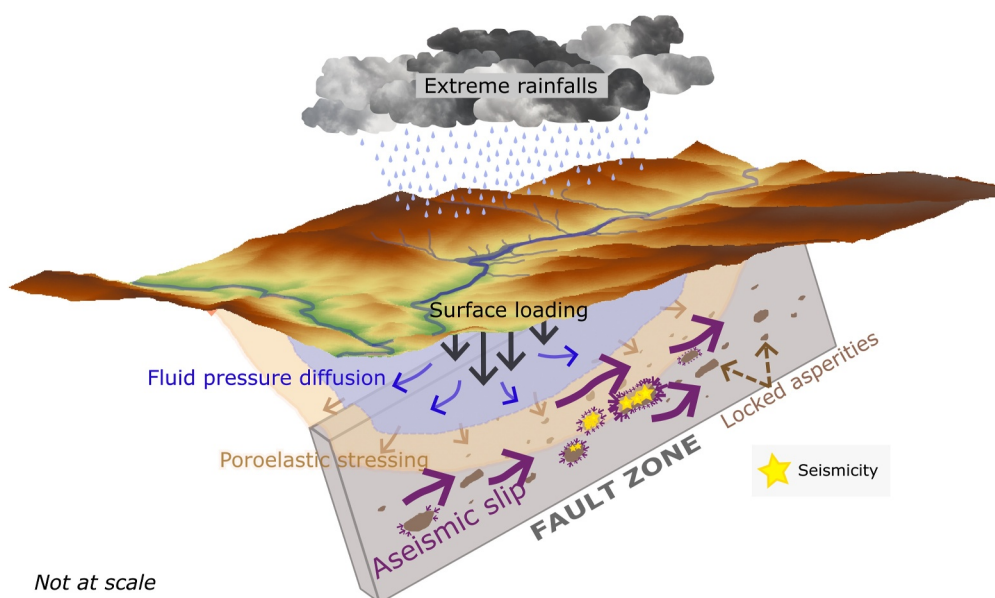


**Figure 11.** Conceptual scheme summarizing the mechanisms underlying the triggering of seismic swarms following the intense rainfall associated with the 2020 Alex extreme storm. The fluid invasion through the fractured medium induces a poroelastic response of the crust at shallow depth, triggering or accelerating aseismic slip on fault planes. As this slip propagated through the fault network, it pressurized and stressed locked asperities, predisposed to rupture and initiated seismic swarm.

sur-Tinée and La Tour. Typically, the landslides have moved soil masses a few hundred meters from their original location. Assuming a soil mobilization thickness ranging from 1 to 3 m (BDMvt database), a volume of displaced materials is estimated to be approximately comprised between 322,461 and 967,383 m<sup>3</sup>. To estimate the impact of these local mass movements, we compare our estimated values with the Le Teil quarry exploitation (South-East of France), suspected of playing a potential role in the triggering of a  $M_w = 4.9$  earthquake at about 1 km in 2019 (Ampuero et al., 2019; Liang & Ampuero, 2021). A Coulomb failure stress change smaller than 150 kPa was reported at 1 km depth due to the quarry's mass removal (Liang & Ampuero, 2021). In our case, assuming similar rock density, the landslides observed in the lower Tinée valley represent only 0.8%–2.3% of the volume of rocks extracted in Le Teil quarry ( $42.3 \times 10^6$  m<sup>3</sup>) (De Novellis et al., 2021; Liang & Ampuero, 2021), resulting in a Coulomb failure stress change significantly smaller than the one reported at 1 km depth in the Le Teil case. This difference is even more pronounced at the 3–4 km depth of observed seismicity in the Tinée. Consequently, the contribution of surface mass movements to the triggering of seismicity is deemed negligible.

The earthquake-earthquake interactions within clusters can lead to co-seismic stress transfer, potentially influencing the swarm behavior. Clusters of small to moderate earthquakes have the capacity to increase Coulomb stress in faults within or adjacent fault segments, bringing them closer to failure. Furthermore, the increase in co-seismic fluid pressure induced by earthquakes can reduce fault resistance. In the present study, the inter-event time distribution of the seismicity detected post the Alex storm (Figure S23 in Supporting Information S1) reveals that a portion of earthquakes occurs within a short time window (<100 s), suggesting potential effects within individual clusters. However, testing this contribution on this intricate swarm sequence poses challenges.

Finally, given that our study highlights that the stress perturbations due to aseismic slip migration appear to be the dominant process, the impact of low surface loadings, such as atmospheric loading and tidal interactions, is deemed negligible.

## 8. Conclusion

The 2020 Alex storm, featuring localized rainfall exceeding 600 mm within a 24-hr span, led to an unprecedented surge in seismic activity in the lower Tinée valley—a region characterized by low background deformation in the southern French Alps. Our study provides evidence of a bi-directional seismicity migration characterized by dual velocities within swarms. The northward seismicity migration aligns with the velocity indicative of aseismic slip,

while the southward migration corresponds to the velocity associated with fluid pressure diffusion. This migration behavior indicates the interplay of multiple physical mechanisms in both triggering and driving seismic events. Comparing a fluid-driven model based on diffusion in a poroelastic medium with a stress-driven model based on rate-and-state friction, we can explain the overall evolution of observed seismicity, and provide insights into the involved mechanisms. While previous studies in other regions around the world have shown that fluid pressure diffusion or surface loading resulting from heavy rainfall can induce seismicity at shallow depths in the crust, our investigation suggests that the sequence of earthquake swarms following the extreme rainfall linked to the 2020 Alex storm may have been triggered by intermittent stress perturbations arising from aseismic slip migration. Our analyses demonstrate that stress changes resulting from fluid pressure diffusion cannot explain the observed seismicity. Nonetheless, the existence of permeable faults beneath the Tinée valley could facilitate the deep transmission of precipitation, potentially triggering or accelerating slow aseismic slip on critically stressed faults within a weakened crust. Thus, our observations and modeling results are consistent with the interpretation of the complex swarm sequence as indicative of the expansion of aseismic slip within a fluid-saturated fault system.

### Data Availability Statement

The detections of the seismic events recorded and analyzed by the seismological observatory of Observatoire de la Côte d'Azur, hosted by the Geoazur laboratory, is available in the following open-source database: <https://sis-moazur.oca.eu> (Geoazur, 2023). The detections of the seismic events are performed on the seismic stations from EPOS-RESIF (RESIF, 1995) and Instituto Nazionale Di Geofisica e Vulcanologia institute (Istituto Nazionale di Geofisica e Vulcanologia (INGV), 2005; University of Genoa, 1967). The geological context (lithology, faults surface traces) is originally provided by the Bureau de Recherches Géologiques et Minières (<https://www.brgm.fr/fr>, 2023) through its online platform Infoterre (<http://infoterre.brgm.fr/>, 2023) where 1/50 000 geological maps are available (Bd Charm-50). GNSS station CGRO data are provided by the RESIF-RENAG French national Geodetic Network: <http://renag.resif.fr/fr/> [<https://doi.org/10.15778/resif.rg>]. NonLinLoc software (Lomax et al., 2000; version 7.00, 27 September 2007; Lomax et al., 2014), providing absolute locations of the seismicity, is available at <http://alomax.free.fr/nlloc/> [[https://doi.org/10.1007/978-94-015-9536-0\\_5](https://doi.org/10.1007/978-94-015-9536-0_5)][[https://doi.org/10.1007/978-3-642-27737-5\\_150-2](https://doi.org/10.1007/978-3-642-27737-5_150-2)]. The double-difference relative relocation has been carried on using HypoDD (version 2.0b, provided by email at [felixw@Ideo.columbia.edu](mailto:felixw@Ideo.columbia.edu)) software from Waldhauser and Ellsworth (2000) [<https://doi.org/10.3133/ofr01113>]. The original version of the software is provided at <https://www.ideo.columbia.edu/~felixw/hypoDD.html>. Rainfall data were freely provided by Clans weather station from Nice Meteo 06 association (<https://meteo06.fr>).

### Acknowledgments

We thank R. Chochon and M. Vidal for providing the meteorological data from Nice Meteo 06 association, C. Petit and F. Leclerc for discussions on the geology of the studied area, F. Courboux and B. Gardonio for discussions on the seismic analysis, and P. Audra for discussions on the karstic environments. This work benefited from the seismic data accessible from Seismoazur database. We thank all the seismological staff members from the Seismological Observatory at Geoazur lab (X. Martin, J. Cheze, D. Brunel, C. Maron, D. Ambrois), who have participated in the installation and maintenance of the seismological networks used in this study. For the modeling part of this work, we acknowledge the financial support by the Agence Nationale de la Recherche (ANR) through the INSeIS project under contract ANR-22-CE49-0018 (PI: L. De Barros, Université Côte d'Azur, France). L. Jacquemond benefits from a financial support of the Université Côte d'Azur. We thank Maria Mesimeri, an anonymous reviewer, and the editor for constructive comments.

### References

- Álvarez-Gómez, J. A. (2019). FMC—Earthquake focal mechanisms data management, cluster and classification. *SoftwareX*, 9, 299–307. <https://doi.org/10.1016/j.softx.2019.03.008>
- Ampuero, J. P., Audin, L., Bernard, P., Brenguier, F., Delouis, B., Grandin, R., et al. (2019). *Rapport d'évaluation du groupe de travail (GT) CNRS-INSU sur le séisme du Teil du 11 novembre 2019 et ses causes possibles. [Rapport de recherche]*. Institut National des Sciences de l'Univers. Retrieved from <https://hal.science/hal-03080941>
- Baietto, A., Perello, P., Cadoppi, P., & Martinotti, G. (2009). Alpine tectonic evolution and thermal water circulations of the Argentera Massif (South-Western Alps). *Swiss Journal of Geosciences*, 102(2), 223–245. <https://doi.org/10.1007/s00015-009-1313-5>
- Baques, M., De Barros, L., Godano, M., Duverger, C., & Jomard, H. (2023). Swarms and mainshock–aftershocks sequences are both triggered by fluids in the Ubaye Region (western Alps). *Geophysical Journal International*, 235(1), 920–941. <https://doi.org/10.1093/gji/ggad280>
- Baroux, E., Béthoux, N., & Bellier, O. (2001). Analyses of the stress field in southeastern France from earthquake focal mechanisms. *Geophysical Journal International*, 145(2), 336–348. <https://doi.org/10.1046/j.1365-246x.2001.01362.x>
- Bettinelli, P., Avouac, J., Flouzat, M., Bollinger, L., Ramillien, G., Rajaure, S., & Sapkota, S. (2008). Seasonal variations of seismicity and geodetic strain in the Himalaya induced by surface hydrology. *Earth and Planetary Science Letters*, 266(3–4), 332–344. <https://doi.org/10.1016/j.epsl.2007.11.021>
- Bhattacharya, P., & Viesca, R. C. (2019). Fluid-induced aseismic fault slip outpaces pore-fluid migration. *Science*, 364(6439), 464–468. <https://doi.org/10.1126/science.aaw7354>
- Bigot-Cormier, F., Sosson, M., Poupeau, G., Stéphan, J.-F., & Labrin, E. (2006). The denudation history of the Argentera Alpine External Crystalline Massif (Western Alps, France-Italy): An overview from the analysis of fission tracks in apatites and zircons. *Geodinamica Acta*, 19(6), 455–473. <https://doi.org/10.3166/ga.19.455-473>
- Bollinger, L., Perrier, F., Avouac, J. P., Sapkota, S., Gautam, U., & Tiwari, D. R. (2007). Seasonal modulation of seismicity in the Himalaya of Nepal. *Geophysical Research Letters*, 34(8), L08304. <https://doi.org/10.1029/2006GL029192>
- Bourouis, S., & Bernard, P. (2007). Evidence for coupled seismic and aseismic fault slip during water injection in the geothermal site of Soutz (France), and implications for seismogenic transients. *Geophysical Journal International*, 169(2), 723–732. <https://doi.org/10.1111/j.1365-246X.2006.03325.x>
- Brigode, P., Vigoureux, S., Delestre, O., Nicolle, P., Payrastré, O., Raphaëlle, D., et al. (2021). Inondations sur la Côte d'Azur: bilan hydro-météorologique des épisodes de 2015 et 2019. *LHB*, 107(1), 1–14. <https://doi.org/10.1080/27678490.2021.1976600>

- Calais, E., Nocquet, J.-M., Jouanne, F., & Tardy, M. (2002). Current strain regime in the western Alps from continuous global positioning system measurements, 1996–2001. *Geology*, 30(7), 651. [https://doi.org/10.1130/0091-7613\(2002\)030<0651:CSRITW>2.0.CO;2](https://doi.org/10.1130/0091-7613(2002)030<0651:CSRITW>2.0.CO;2)
- Cappa, F., Maria Scuderi, M., Collettini, C., Guglielmi, Y., & Avouac, J. P. (2019). Stabilization of fault slip by fluid injection in the laboratory and in situ. *Science Advances*, 5(3). <https://doi.org/10.1126/sciadv.aau4065>
- Cappa, F., Rutqvist, J., & Yamamoto, K. (2009). Modeling crustal deformation and rupture processes related to upwelling of deep CO<sub>2</sub>-rich fluids during the 1965–1967 Matsushiro earthquake swarm in Japan. *Journal of Geophysical Research*, 114(B10), B10304. <https://doi.org/10.1029/2009JB006398>
- Carrega, P., & Michelot, N. (2021). Une catastrophe hors norme d'origine météorologique le 2 octobre 2020 dans les montagnes des Alpes-Maritimes. *Physio-Géo*, 16, 1–70. <https://doi.org/10.4000/physio-geo.12370>
- Chen, L., & Talwani, P. (2001). Mechanism of initial seismicity following impoundment of the Monticello Reservoir, South California. *Bulletin of the Seismological Society of America*, 91(6), 1582–1594. <https://doi.org/10.1785/0120000293>
- Chen, X., Shearer, P. M., & Abercrombie, R. E. (2012). Spatial migration of earthquakes within seismic clusters in Southern California: Evidence for fluid diffusion. *Journal of Geophysical Research*, 117(B4), B04301. <https://doi.org/10.1029/2011JB008973>
- Chmiel, M., Godano, M., Piantini, M., Brigode, P., Gimbert, F., Bakker, M., et al. (2022). Seismological analysis of flood dynamics and hydrologically triggered earthquake swarms associated with Storm Alex. *Natural Hazards Earth System Sciences*, 22(5), 1541–1558. <https://doi.org/10.5194/nhess-22-1541-2022>
- Christiansen, L. B., Hurwitz, S., & Ingebrigt, S. E. (2007). Annual modulation of seismicity along the San Andreas Fault near Parkfield, CA. *Geophysical Research Letters*, 34(4), L04306. <https://doi.org/10.1029/2006GL028634>
- Costain, J. K. (2017). Groundwater recharge as the trigger of naturally occurring intraplate earthquakes. *Geological Society London Special Publications*, 432(1), 91–118. <https://doi.org/10.1144/SP432.9>
- Costain, J. K., & Bollinger, G. A. (2010). Review: Research results in hydroseismicity from 1987 to 2009. *Bulletin of the Seismological Society of America*, 100(5A), 1841–1858. <https://doi.org/10.1785/0120090288>
- Costain, J. K., Bollinger, G. A., & Speer, J. A. (1987). Hydroseismicity—A hypothesis for the role of water in the generation of intraplate seismicity. *Geology*, 15(7), 618–621. [https://doi.org/10.1130/0091-7613\(1987\)15<618:HHFTR0>2.0.CO;2](https://doi.org/10.1130/0091-7613(1987)15<618:HHFTR0>2.0.CO;2)
- Coward, M., & Dietrich, D. (1989). Alpine tectonics: An overview. *Geological Society of London Special Publication*, 45(1), 1–29. <https://doi.org/10.1144/GSL.SP.1989.045.01.01>
- Craig, T. J., Chanard, K., & Calais, E. (2017). Hydrologically-driven crustal stresses and seismicity in the New Madrid Seismic Zone. *Nature Communications*, 8(1), 2143. <https://doi.org/10.1038/s41467-017-01696-w>
- D'Agostino, N., Silverii, F., Amoroso, O., Convertito, V., Fiorillo, F., Ventafriidda, G., & Zollo, A. (2018). Crustal deformation and seismicity modulated by groundwater recharge of karst aquifers. *Geophysical Research Letters*, 45(22), 12253–12262. <https://doi.org/10.1029/2018GL079794>
- Danré, P., De Barros, L., Cappa, F., & Ampuero, J.-P. (2022). Prevalence of aseismic slip linking fluid injection to natural and anthropogenic seismic swarms. *Journal of Geophysical Research: Solid Earth*, 127(12), e2022JB025571. <https://doi.org/10.1029/2022JB025571>
- De Barros, L., Baques, M., Godano, M., Helmstetter, A., Deschamps, A., Larroque, C., & Courboulex, F. (2019). Fluid-induced swarms and coseismic stress transfer: A dual process highlighted in the aftershock sequence of the 7 April 2014 earthquake (M<sub>L</sub> 4.8, Ubaye, France). *Journal of Geophysical Research: Solid Earth*, 124(4), 3918–3932. <https://doi.org/10.1029/2018JB017226>
- De Barros, L., Cappa, F., Deschamps, A., & Dublanche, P. (2020). Imbricated aseismic slip and fluid diffusion drive a seismic swarm in the Corinth Gulf, Greece. *Geophysical Research Letters*, 47(9), e2020GL087142. <https://doi.org/10.1029/2020GL087142>
- De Barros, L., Guglielmi, Y., Rivet, D., Cappa, F., & Dubouef, L. (2018). Seismicity and fault aseismic deformation caused by fluid injection in decametric in-situ experiments. *Comptes Rendus Geoscience*, 350(8), 464–475. <https://doi.org/10.1016/j.crte.2018.08.002>
- De Barros, L., Wynants-Morel, N., Cappa, F., & Danré, P. (2021). Migration of fluid-induced seismicity reveals the seismogenic state of faults. *Journal of Geophysical Research: Solid Earth*, 126(11), e2021JB022767. <https://doi.org/10.1029/2021JB022767>
- Delrieu, G., Nicol, J., Yates, E., Kirstetter, P., Creutin, J., Anquetin, S., et al. (2005). The catastrophic flash-flood event of 8–9 September 2002 in the Gard Region, France: A first case study for the Cévennes–Vivarais Mediterranean hydrometeorological observatory. *Journal of Hydro-meteorology*, 6(1), 34–52. <https://doi.org/10.1175/jhm-400.1>
- De Novellis, V., Convertito, V., Valkaniotis, S., Casu, F., Lanari, R., Monterroso Tobar, M. F., & Pino, N. A. (2021). Author correction: Coincident locations of rupture nucleation during the 2019 Le Teil earthquake, France and maximum stress change from local cement quarrying. *Communications Earth & Environment*, 2(1), 47. <https://doi.org/10.1038/s43247-021-00109-7>
- Dercourt, J., Zonenshain, L. P., Ricou, L.-E., Kazmin, V. G., Le Pichon, X., Knipper, A. L., et al. (1986). Geological evolution of the Tethys Belt from the Atlantic to the Pamirs since the Lias. *Tectonophysics*, 123(1–4), 241–315. [https://doi.org/10.1016/0040-1951\(86\)90199-X](https://doi.org/10.1016/0040-1951(86)90199-X)
- Derode, B., Gounon, A., Letort, J., Sylvander, M., Rigo, A., Benahmed, S., et al. (2023). Fluid-driven seismic swarms in the Gripp valley (Haute-Pyrénées, France). *Geophysical Journal International*, 234(3), 1903–1915. <https://doi.org/10.1093/gji/ggad175>
- Dieterich, J. (1994). A constitutive law for rate of earthquake production and its application to earthquake clustering. *Journal of Geophysical Research*, 99(B2), 2601–2618. <https://doi.org/10.1029/93jb02581>
- Dietze, M., Hoffmann, T., Bell, R., Schrott, L., & Hovius, N. (2022). A seismic approach to flood detection and characterization in upland catchments. *Geophysical Research Letters*, 49(20), e2022GL100170. <https://doi.org/10.1029/2022GL100170>
- Dumont, T., Schwartz, S., Guillot, S., Malusà, M., Jouvent, M., Monié, P., & Verly, A. (2022). Cross-propagation of the western Alpine orogen from early to late deformation stages: Evidence from the Internal Zones and implications for restoration. *Earth-Science Reviews*, 232, 104106. <https://doi.org/10.1016/j.earscirev.2022.104106>
- Dura-Gomez, I., & Talwani, P. (2010). Reservoir-induced seismicity associated with the Itoiz Reservoir, Spain: A case study. *Geophysical Journal International*, 181(1), 343–356. <https://doi.org/10.1111/j.1365-246X.2009.04462.x>
- Eva, E., Malusà, M. G., & Solarino, S. (2020). Seismotectonics at the transition between opposite-dipping slabs (western Alpine region). *Tectonics*, 39(9), e2020TC006086. <https://doi.org/10.1029/2020TC006086>
- Eva, E., Solarino, S., & Spallarossa, D. (2001). Seismicity and crustal structure beneath the western Ligurian Sea derived from local earthquake tomography. *Tectonophysics*, 339(3–4), 495–510. [https://doi.org/10.1016/S0040-1951\(01\)00106-8](https://doi.org/10.1016/S0040-1951(01)00106-8)
- Eyre, T. S., Eaton, D. W., Zecevic, M., D'Amico, D., & Kolos, D. (2019). Microseismicity reveals fault activation before Mw 4.1 hydraulic-fracturing induced earthquake. *Geophysical Journal International*, 218(1), 534–546. <https://doi.org/10.1093/gji/ggz168>
- Faure-Muret, A. (1957). Notice de la carte géologique au 1/50 000 de Puget Thénier n°946. Edition BRGM.
- Fehlberg, E. (1969). Low-order classical Runge-Kutta formulas with stepsize control and their application to some heat transfer problems. *National Aeronautics and Space Administration Technical Report*, 315.
- Foulger, G. R., Wilson, M. P., Gluyas, J. G., Julian, B. R., & Davies, R. J. (2018). Global review of human-induced earthquakes. *Earth-Science Reviews*, 178, 438–514. <https://doi.org/10.1016/j.earscirev.2017.07.008>



- Gao, H., Schmidt, D. A., & Weldon, R. J. (2012). Scaling relationships of source parameters for slow slip events. *Bulletin of Seismological Society of America*, 102(1), 352–360. <https://doi.org/10.1785/0120110096>
- Gao, S., Silver, P., Linde, A., & Sacks, S. (2000). Annual modulation of triggered seismicity following the 1992 Landers earthquake in California. *Nature*, 406(6795), 500–504. <https://doi.org/10.1038/35020045>
- Gattacceca, J., Deino, A., Rizzo, R., Jones, D. S., Henry, B., Beaudoin, B., & Valeboin, F. (2007). Miocene rotation of Sardinia: New paleomagnetic and geochronological constraints and geodynamic implications. *Earth and Planetary Science Letters*, 258(3–4), 359–377. <https://doi.org/10.1016/j.epsl.2007.02.003>
- Gibbons, S. J., & Ringdal, F. (2006). The detection of low magnitude seismic events using array-based waveform correlation. *Geophysical Journal International*, 165(1), 149–166. <https://doi.org/10.1111/j.1365-246X.2006.02865.x>
- Godano, M., Deschamps, A., Lambotte, S., Lyon-Caen, H., Bernard, P., & Pacchiani, F. (2014). Focal mechanisms of earthquake multiplets in the western part of the Corinth Rift (Greece): Influence of the velocity model and constraints on the geometry of the active faults. *Geophysical Journal International*, 197(3), 1660–1680. <https://doi.org/10.1093/gji/ggu059>
- Godano, M., Larroque, C., Bertrand, E., Courboux, F., Deschamps, A., Salichon, J., et al. (2013). The October–November 2010 earthquake swarm near Sampeyre (Piedmont region, Italy): A complex multicluster sequence. *Tectonophysics*, 608, 97–111. <https://doi.org/10.1016/j.tecto.2013.10.010>
- Godano, M., Regnier, M., Deschamps, A., Bardainne, T., & Gaucher, E. (2009). Focal mechanisms from sparse observations by nonlinear inversion of amplitudes: Method and tests on synthetic and real data. *Bulletin of the Seismological Society of America*, 99(4), 2243–2264. <https://doi.org/10.1785/0120080210>
- Guglielmi, Y., Cappa, F., Avouac, J.-P., Henry, P., & Elsworth, D. (2015). Seismicity triggered by fluid injection–induced aseismic slip. *Science*, 348(6240), 1224–1226. <https://doi.org/10.1126/science.aab0476>
- Hainzl, S. (2004). Seismicity patterns of earthquake swarms due to fluid intrusion and stress triggering. *Geophysical Journal International*, 159(3), 1090–1096. <https://doi.org/10.1111/j.1365-246X.2004.02463.x>
- Hainzl, S., Ben-Zion, Y., Cattania, C., & Wassermann, J. (2013). Testing atmospheric and tidal earthquake triggering at Mt. Hochstaufen, Germany. *Journal of Geophysical Research: Solid Earth*, 118(10), 5442–5452. <https://doi.org/10.1002/jgrb.50387>
- Hainzl, S., & Christophersen, A. (2017). Testing alternative temporal aftershock decay functions in an ETAS framework. *Geophysical Journal International*, 210(2), 585–593. <https://doi.org/10.1093/gji/ggx184>
- Hainzl, S., Christophersen, A., Rhoades, D., & Harte, D. (2016). Statistical estimation of the duration of aftershock sequences. *Geophysical Journal International*, 205(2), 1180–1189. <https://doi.org/10.1093/gji/ggw075>
- Hainzl, S., Kraft, T., Wassermann, J., Igel, H., & Schmedes, E. (2006). Evidence for rain-triggered earthquake activity. *Geophysical Research Letters*, 33(19), L19303. <https://doi.org/10.1029/2006GL027642>
- Hainzl, S., & Ogata, Y. (2005). Detecting fluid signals in seismicity data through statistical earthquake modeling. *Journal of Geophysical Research*, 110(B5), B05S07. <https://doi.org/10.1029/2004JB003247>
- Handy, M. R., Schmid, S. M., Bousquet, R., Kissling, E., & Bernoulli, D. (2010). Reconciling plate-tectonic reconstructions of Alpine Tethys with the geological–geophysical record of spreading and subduction in the Alps. *Earth-Science Reviews*, 102(3–4), 121–158. <https://doi.org/10.1016/j.earscirev.2010.06.002>
- Hanka, W., Saul, J., Weber, B., Becker, J., Harjadi, P., & Fauzi, & GITEWS Seismology Group. (2010). Real-time earthquake monitoring for tsunami warning in the Indian Ocean and beyond. *Natural Hazards Earth System Sciences*, 10(12), 2611–2622. <https://doi.org/10.5194/nhess-10-2611-2010>
- Hardebeck, J. L. (2012). Fluid-driven seismicity response of the Rinconada Fault near Paso Robles, California, to the 2003 M 6.5 San Simeon earthquake. *Bulletin of the Seismological Society of America*, 102(1), 377–390. <https://doi.org/10.1785/0120110169>
- Hardebeck, J. L., & Michael, A. J. (2006). Damped regional-scale stress inversions: Methodology and examples for southern California and the Coalinga aftershock sequence. *Journal of Geophysical Research*, 111(B11), B11310. <https://doi.org/10.1029/2005JB004144>
- Harrington, L. J., Dean, S. M., Awatere, S., Rosier, S., Queen, L., Gibson, P. B., et al. (2023). The role of climate change in extreme rainfall associated with Cyclone Gabrielle over Aotearoa New Zealand’s East Coast. *World Weather Attribution Initiative Scientific*. <https://doi.org/10.25561/102624>
- Hatch, R. L., Abercrombie, R. E., Ruhl, C. J., & Smith, K. D. (2020). Evidence of aseismic and fluid-driven processes in a small complex seismic swarm near Virginia City, Nevada. *Geophysical Research Letters*, 47(4), e2019GL085477. <https://doi.org/10.1029/2019GL085477>
- Heimisson, E. R., & Segall, P. (2018). Constitutive law for earthquake production based on rate-and-state friction: Dieterich 1944 revisited. *Journal of Geophysical Research: Solid Earth*, 123(5), 4141–4156. <https://doi.org/10.1029/2018JB015656>
- Heimisson, E. R., & Segall, P. (2020). Physically consistent modeling of dike-induced deformation and seismicity: Application to the 2014 Bårðarbunga dike, Iceland. *Journal of Geophysical Research: Solid Earth*, 125(2), e2019JB018141. <https://doi.org/10.1029/2019JB018141>
- Hsu, Y.-J., Kao, H., Bürgmann, R., Lee, Y.-T., Huang, H.-H., Hsu, Y.-F., et al. (2021). Synchronized and asynchronous modulation of seismicity by hydrological loading: A case study in Taiwan. *Science Advances*, 7(16). <https://doi.org/10.1126/sciadv.abf7282>
- Husen, S., Bachmann, C., & Giardini, D. (2007). Locally triggered seismicity in central Swiss Alps following the large rainfall event of August 2005. *Geophysical Journal International*, 171(3), 1126–1134. <https://doi.org/10.1111/j.1365-246X.2007.03561.x>
- Istituto Nazionale di Geofisica e Vulcanologia (INGV). (2005). *Rete Sismica Nazionale (RSN)*. Istituto Nazionale di Geofisica e Vulcanologia (INGV). <https://doi.org/10.13127/SD/X0FXnH7QFY>
- Jaeger, J. C., Cook, N. G. W., & Zimmerman, R. W. (2007). *Fundamentals of rock mechanics* (4e edition, p. 488). Wiley. <https://doi.org/10.1017/CBO978051173549>
- Johnson, C. W., Fu, Y., & Bürgmann, R. (2017a). Stress models of the annual hydrospheric, atmospheric, thermal, and tidal loading cycles on California faults: Perturbation of background stress and changes in seismicity: Stress models of annual loading cycles. *Journal of Geophysical Research: Solid Earth*, 122(12), 10605–10625. <https://doi.org/10.1002/2017JB014778>
- Johnson, C. W., Fu, Y. N., & Bürgmann, R. (2017b). Seasonal water storage, stress modulation, and California seismicity. *Science*, 356(6343), 1161–1164. <https://doi.org/10.1126/science.aak9547>
- Jolivet, L., Augier, R., Faccenna, C., Negro, F., Rimmel, G., Agard, P., et al. (2008). Subduction, convergence and the mode of backarc extension in the Mediterranean region. *Bulletin de la Société Géologique de France*, 179(6), 525–550. <https://doi.org/10.2113/gssgfbull.179.6.525>
- Kennett, B. L. N., & Engdahl, E. R. (1991). Travel times for global earthquake location and phase association. *Geophysical Journal International*, 105(2), 429–465. <https://doi.org/10.17611/DP/9991809>
- Kirkpatrick, S., Gelatt, C. D. J. R., & Vecchi, M. P. (1983). Optimization by simulated annealing. *Science*, 220(4598), 671–680. <https://doi.org/10.1126/science.220.4598.671>
- Kraft, T., Wassermann, J., & Igel, H. (2006). High-precision relocation and focal mechanism of the 2002 rain-triggered earthquake swarm at Mt. Hochstaufen, SE Germany. *Geophysical Journal International*, 167(3), 1513–1528. <https://doi.org/10.1111/j.1365-246X.2006.03171.x>

- Kraft, T., Wassermann, J., Schmedes, E., & Igel, H. (2006). Meteorological triggering of earthquake swarms at Mt. Hochstaufen, SE-Germany. *Tectonophysics*, 424(3–4), 245–258. <https://doi.org/10.1016/j.tecto.2006.03.044>
- Larroque, C., Baize, S., Albaric, J., Jomard, H., Trévisan, J., Godano, M., et al. (2021). Seismotectonics of southeast France: From the Jura mountains to Corsica. *Comptes Rendus. Géoscience*, 353(S1), 105–151. <https://doi.org/10.5802/crgeos.69>
- Larroque, C., Béthoux, N., Calais, E., Courboulex, F., Deschamps, A., Déverchère, J., et al. (2001). Active deformation at the junction between southern French Alps and Ligurian basin. *Geologie en Mijnbouw*, 80(3–4), 255–272. <https://doi.org/10.1017/s0016774600023878>
- Larroque, C., Delouis, B., Godel, B., & Nocquet, J.-M. (2009). Active deformation at the southwestern Alps–Ligurian basin junction (France–Italy boundary): Evidence for recent change from compression to extension in the Argentera Massif. *Tectonophysics*, 467(1–4), 22–34. <https://doi.org/10.1016/j.tecto.2008.12.013>
- Lengliné, O., Frank, W. B., Marsan, D., & Ampuero, J. P. (2017). Imbricated slip rate processes during slow slip transients imaged by low-frequency earthquakes. *Earth and Planetary Science Letters*, 476, 122–131. <https://doi.org/10.1016/j.epsl.2017.07.032>
- Li, S., & Otto, F. (2022). The role of human-induced climate change in heavy rainfall events such as the one associated with Typhoon Hagibis. *Climatic Change*, 172(7), 7. <https://doi.org/10.1007/s10584-022-03344-9>
- Liang, C., & Ampuero, J. P. (2021). Comment on “Coincident locations of rupture nucleation during the 2019 Le Teil earthquake, France, and maximum stress changes from local cement quarrying” by Novellis et al. *Communications Earth & Environment*.
- Liu, S., Xu, L., & Talwani, P. (2011). Reservoir-induced seismicity in the Danjiangkou Reservoir: A quantitative analysis. *Geophysical Journal International*, 185(1), 514–528. <https://doi.org/10.1111/j.1365-246X.2011.04959.x>
- Llenos, A. L., McGuire, J. J., & Ogata, Y. (2009). Modeling seismic swarms triggered by aseismic transients. *Earth and Planetary Science Letters*, 281(1–2), 59–69. <https://doi.org/10.1016/j.epsl.2009.02.011>
- Lohman, R. B., & McGuire, J. J. (2007). Earthquake swarms driven by aseismic creep in the Salton Trough, California. *Journal of Geophysical Research*, 112(B4), B04405. <https://doi.org/10.1029/2006JB04596>
- Lomax, A., Michelini, A., & Curtis, A. (2014). Earthquake location, direct, global-search methods. In R. Meyers (Ed.), *Encyclopedia of complexity and systems science*. Springer. [https://doi.org/10.1007/978-3-642-27737-5\\_150-2](https://doi.org/10.1007/978-3-642-27737-5_150-2)
- Lomax, A., Virieux, J., Volant, P., & Berge-Thierry, C. (2000). Probabilistic earthquake location in 3D and layered models. In C. H. Thurber, & N. Rabinowitz (Eds.), *Advances in seismic event location, Modern approaches in geophysics* (Vol. 18, pp. 101–134). Springer. [https://doi.org/10.1007/978-94-015-9536-0\\_5](https://doi.org/10.1007/978-94-015-9536-0_5)
- Luu, K., Schoenball, M., Oldenburg, C. M., & Rutqvist, J. (2022). Coupled hydromechanical modeling of induced seismicity from CO<sub>2</sub> injection in the Illinois Basin. *Journal of Geophysical Research: Solid Earth*, 127(5), e2021JB023496. <https://doi.org/10.1029/2021JB023496>
- Marone, C. (1998). Laboratory-derived friction laws and their application to seismic faulting. *Annual Review of Earth and Planetary Sciences*, 26(1), 643–696. <https://doi.org/10.1146/annurev.earth.26.1.643>
- Martínez-Garzón, P., Kwiatak, G., Ickrath, M., & Bohnhoff, M. (2014). MSATSI: A MATLAB package for stress inversion combining solid classic methodology, a new simplified user-handling, and a visualization tool. *Seismological Research Letters*, 85(4), 896–904. <https://doi.org/10.1785/0220130189>
- Masson, C., Mazzotti, S., Vernant, P., & Doerflinger, E. (2019). Extracting small deformation beyond individual station precision from dense Global Navigation Satellite System (GNSS) networks in France and western Europe. *Solid Earth*, 10(6), 1905–1920. <https://doi.org/10.5194/se-10-1905-2019>
- Métivier, L., De Viron, O., Conrad, C. P., Renault, S., Diament, M., & Patau, G. (2009). Evidence of earthquake triggering by the solid Earth tides. *Earth and Planetary Science Letters*, 278(3–4), 370–375. <https://doi.org/10.1016/j.epsl.2008.12.024>
- Miller, S. A. (2008). Note on rain-triggered earthquakes and their dependence on karst geology. *Geophysical Journal International*, 173(1), 334–338. <https://doi.org/10.1111/j.1365-246X.2008.03735.x>
- Miller, S. A. (2013). The role of fluids in tectonic and earthquake processes. *Advances in Geophysics*, 54, 1–46. <https://doi.org/10.1016/b978-0-12-380940-7.00001-9>
- Montgomery-Brown, E. K., Shelly, D. R., & Hsieh, P. A. (2019). Snowmelt-triggered earthquake swarms at the margin of Long Valley Caldera, California. *Geophysical Research Letters*, 46(7), 3698–3705. <https://doi.org/10.1029/2019GL082254>
- Nocquet, J.-M. (2012). Present-day kinematics of the Mediterranean: A comprehensive overview of GPS results. *Tectonophysics*, 579, 220–242. <https://doi.org/10.1016/j.tecto.2012.03.037>
- Perrochet, L., Preisig, G., & Valley, B. (2023). Quantifying the mechanisms of rain-triggered seismicity in karstic regions. *Frontiers in Earth Science*, 11. <https://doi.org/10.3389/feart.2023.1234856>
- Reid, H. F. (1911). *The elastic-rebound theory of earthquakes* (Vol. 6, pp. 413–444). University of California Publications. Bulletin of the Department of Geological Sciences.
- RESIF. (1995). RESIF-RLBP French Broad-band network, RESIF-RAP strong motion network and other seismic stations in metropolitan France. *RESIF—Réseau Sismologique et géodésique Français*. <https://doi.org/10.15778/resif.fr>
- Ribes, A., Thao, S., Vautard, R., Dubuisson, B., Somot, S., Colin, J., et al. (2019). Observed increase in extreme daily rainfall in the French Mediterranean. *Climate Dynamics*, 52(1–2), 1095–1114. <https://doi.org/10.1007/s00382-018-4179-2>
- Rigo, A., Béthoux, N., Masson, F., & Ritz, J. F. (2008). Seismicity rate and wave-velocity variations as consequences of rainfall: The case of the catastrophic storm of September 2002 in the Nîmes fault region (Gard, France). *Geophysical Journal International*, 173(2), 473–482. <https://doi.org/10.1111/j.1365-246X.2008.03718.x>
- Rinaldi, A. P., Improta, L., Hainzl, S., Catali, F., Urpi, L., & Wiemer, S. (2020). Combined approach of poroelastic and earthquake nucleation applied to the reservoir-induced seismic activity in the Val d’Agri area, Italy. *Journal of Rock Mechanics and Geotechnical Engineering*, 12(4), 802–810. <https://doi.org/10.1016/j.jrmge.2020.04.003>
- Ritz, J. F. (1992). Tectonique récente et sismotectonique des Alpes du Sud: Analyses en termes de contraintes. *Quaternaire*, 3, 111–124. <https://doi.org/10.3406/quate.1992.1980>
- Roeloffs, E. A. (1988). Fault stability changes induced beneath a reservoir with cyclic variations in water level. *Journal of Geophysical Research*, 93(B3), 2017–2124. <https://doi.org/10.1029/B093iB03p02107>
- Roland, E., & McGuire, J. J. (2009). Earthquake swarms on transform faults. *Geophysical Journal International*, 178(3), 1677–1690. <https://doi.org/10.1111/j.1365-246X.2009.04214.x>
- Roth, P., Pavoni, N., & Deichmann, N. (1992). Seismotectonics of the eastern Swiss Alps and evidence for precipitation-induced variations of seismic activity. *Tectonophysics*, 207(1–2), 183–197. [https://doi.org/10.1016/0040-1951\(92\)90477-N](https://doi.org/10.1016/0040-1951(92)90477-N)
- Saar, M. O., & Manga, M. (2003). Seismicity induced by seasonal groundwater recharge at Mt. Hood, Oregon. *Earth and Planetary Science Letters*, 214(3–4), 605–618. [https://doi.org/10.1016/S0012-821X\(03\)00418-7](https://doi.org/10.1016/S0012-821X(03)00418-7)
- Scholz, C. H. (2019). *The mechanics of earthquakes and faulting*. Cambridge University Press.

- Scholz, C. H., Tan, Y. J., & Albino, F. (2019). The mechanism of tidal triggering of earthquakes at mid-ocean ridges. *Nature Communications*, *10*(1), 2526. <https://doi.org/10.1038/s41467-019-10605-2>
- Segall, P., Desmarais, E. K., Shelly, D., Miklius, A., & Cervelli, P. (2006). Earthquakes triggered by silent slip events on Kilauea volcano, Hawaii. *Nature*, *442*(6), 71–74. <https://doi.org/10.1038/nature04938>
- Segall, P., & Lu, S. (2015). Injection-induced seismicity: Poroelastic and earthquake nucleation effects. *Journal of Geophysical Research: Solid Earth*, *120*(7), 5082–5103. <https://doi.org/10.1002/2015JB012060>
- Simpson, G. (2001). Influence of compression-induced fluid pressures on rock strength in the brittle crust. *Journal of Geophysical Research*, *106*(B9), 19465–19478. <https://doi.org/10.1029/2001JB000314>
- Sirorattanakul, K., Ross, Z. E., Khoshmanesh, M., Cochran, E. S., Acosta, M., & Avouac, J.-P. (2022). The 2020 Westmorland, California earthquake swarm as aftershocks of a slow slip event sustained by fluid flow. *Journal of Geophysical Research: Solid Earth*, *127*(11), e2022JB024693. <https://doi.org/10.1029/2022JB024693>
- Skempton, A. W. (1954). The pore pressure coefficients A and B. *Geotechnique*, *4*, 143–147. <https://doi.org/10.1680/geot.1954.4.4.143>
- Stampfli, G., Mosar, J., Marquer, D., Marchant, R., Baudin, T., & Borel, G. (1998). Subduction and obduction processes in the Swiss Alps. *Tectonophysics*, *296*(1–2), 159–204. [https://doi.org/10.1016/S0040-1951\(98\)00142-5](https://doi.org/10.1016/S0040-1951(98)00142-5)
- Sue, C., & Tricart, P. (2003). Neogene to ongoing normal faulting in the inner western Alps: A major evolution of the late alpine tectonics. *Tectonics*, *22*(5), 1050. <https://doi.org/10.1029/2002TC001426>
- Talwani, P. (1997). On the nature of reservoir-induced seismicity. *Pure and Applied Geophysics*, *150*(3–4), 473–492. <https://doi.org/10.1007/s000240050089>
- Townend, J., & Zoback, M. D. (2000). How faulting keeps the crust strong. *Geology*, *28*(5), 399–402. [https://doi.org/10.1130/0091-7613\(2000\)28<399:HFKTCS>2.0.CO;2](https://doi.org/10.1130/0091-7613(2000)28<399:HFKTCS>2.0.CO;2)
- University of Genoa. (1967). Regional seismic network of north western Italy [Dataset]. *International Federation of Digital Seismograph Networks*. <https://doi.org/10.7914/SN/GU>
- Utsu, T., Ogata, Y., Matsuura, R., & Matsu'ura (1995). The centenary of the Omori formula for a decay law of aftershocks activity. *Journal of Physics of the Earth*, *43*, 1–33. <https://doi.org/10.4294/jpe1952.43.1>
- Waldhauser, F., & Ellsworth, W. (2000). A double-difference earthquake location algorithm: Method and application to the northern Hayward Fault, California. *Bulletin of the Seismological Society of America*, *90*(6), 1353–1368. <https://doi.org/10.1785/0120000006>
- Walpersdorf, A., Pinget, L., Vernant, P., Sue, C., & Deprez, A., & the RENAG team. (2018). Does long-term GPS in the western Alps finally confirm earthquake mechanisms? *Tectonics*, *37*(10), 3721–3737. <https://doi.org/10.1029/2018TC005054>
- Wang, C.-C., & Nguyen, D. V. (2023). Investigation of an extreme rainfall event during 8–12 December 2018 over central Vietnam—Part 1: Analysis and cloud-resolving simulation. *Natural Hazards Earth System Sciences*, *23*(2), 771–788. <https://doi.org/10.5194/nhess-23-771-2023>
- Wei, S., Avouac, J.-P., Hudnut, K. W., Donnellan, A., Parker, J. W., Graves, R. W., et al. (2015). The 2012 Brawley swarm triggered by injection-induced aseismic slip. *Earth and Planetary Science Letters*, *422*, 115–125. <https://doi.org/10.1016/j.epsl.2015.03.054>
- Wilson, M. P., Foulger, G. R., Saville, C., Graham, S. P., & Julian, B. R. (2022). Earthquake weather and climate change: Should we stress about the forecast? In G. R. Foulger, L. C. Hamilton, D. M. Jurdy, C. A. Stein, K. A. Howard, & S. Stein, (Eds.), *The footsteps of Warren B. Hamilton: New ideas in Earth science*. (Vol. 553, pp. 177–192). Geological Society of America Special Paper. [https://doi.org/10.1130/2021.2553\(15\)](https://doi.org/10.1130/2021.2553(15))
- Woollam, J., Münchmeyer, J., Tilmann, F., Rietbrock, A., Lange, D., Bornstein, T., et al. (2022). SeisBench—A toolbox for machine learning in seismology. *Seismological Research Letters*, *93*(3), 1695–1709. <https://doi.org/10.1785/0220210324>
- Wynants-Morel, N., Cappa, F., De Barros, L., & Ampuero, J.-P. (2020). Stress perturbation from aseismic slip drives the seismic front during fluid injection in a permeable fault. *Journal of Geophysical Research: Solid Earth*, *125*(7), e2019JB019179. <https://doi.org/10.1029/2019JB019179>
- Yoshida, K., & Hasegawa, A. (2018). Sendai-Okura earthquake swarm induced by the 2011 Tohoku-Oki earthquake in the stress shadow of NE Japan: Detailed fault structure and hypocenter migration. *Tectonophysics*, *733*, 132–147. <https://doi.org/10.1016/j.tecto.2017.12.031>
- Yukutake, Y., Yoshida, K., & Honda, R. (2022). Interaction between aseismic slip and fluid invasion in earthquake swarms revealed by dense geodetic and seismic observations. *Journal of Geophysical Research: Solid Earth*, *127*(4), e2021JB022933. <https://doi.org/10.1029/2021JB022933>
- Zhuang, J., Harte, D. S., Werner, M. J., Hainzl, S., & Zhou, S. (2012). Basic models of seismicity: Temporal models. *Community Online Resource for Statistical Seismicity Analysis*. <https://doi.org/10.5078/corssa-79905851>